UCLouvain

École polytechnique de Louvain

Alleviating solicitations on yaw actuators using individual pitch control for wake redirection in wind farm control

Authors : Thomas **GIORGIO**
Supervisors : **Phillipe CHATELAIN**
Readers : **Matthieu DUPONCHEEL**, **Paul FISETTE**
Academic year 2022–2023
Master [120] Mechanical Engineering

Abstract

A wind turbine has become one of the solutions to create clean energy. Different strategies to optimize power production in a wind farm have been studied and investigated. Yaw misalignment is one of many promising strategies. Nevertheless, commercial wind turbines rely on yaw actuators to achieve yaw misalignment. Yaw actuators are subjected to fatigue loads and hence reduce the lifetime of the wind turbine. This master thesis investigates a free-yaw wind turbine where the yawing mechanism can be achieved by creating load imbalances in the blades of a wind turbine through a yaw controller. The study is done through a numerical simulation with an accurate LES Vortex Particle-Mesh solver. The free-yaw wind turbine is compared to a fix-yaw wind turbine with and without load-alleviating IPC. The study covers its power production, the wake that it produces, and the load acting on the wind turbine. Two different strategies are analyzed. First, the wind turbine is subjected to a static yaw input misalignment, and second, the wind turbine is subjected to a dynamic yaw input misalignment. In the end, the first strategy appears to be more promising to be implemented.

Acknowledgement

First of all, I would like to thank Professor Phillipe Chatelain, the promotor of this master's thesis. I would also like to thank Jean-Baptiste Crismer. He guided and followed my journey in creating this master's thesis, more than that, his input kept me away from making stupid mistakes. I would also like to thank to Marion Coquelet, who helped me with installing the VPM and debugging it. Moreover, I would like to thank other staff at IMMC who spared their time to listen to my presentation and show the way when I encountered problems

I would like to thank my family and relatives, especially my father, Vincent, and my two sisters, Theresa and Tamara, to whom I always tell my problems throughout my study. I especially want to thank my mom, who sent me to study abroad, where I can have priceless experiences. Without her, I would never be here. I also want to thank my friends, here and back home, who have kept me in company. I hope that this master's thesis may contribute to the wind energy field.

Computational resources have been provided by the supercomputing facilities of the Université catholique de Louvain (CISM/UCL) and the Consortium des Équipements de Calcul Intensif en Fédération Wallonie Bruxelles (CÉCI) funded by the Fonds de la Recherche Scientifique de Belgique (F.R.S.-FNRS) under convention 2.5020.11 and by the Walloon Region.

Contents

Appendices

Chapter 1

Introduction

1.1 Context and motivations

In the last two decades, climate change has been a hot topic in our modern society. The increasing demand for energy raises the production of greenhouse gases. The *2030 Climate Target Plan*, as part of the green deal, targeted to cut greenhouse gas emissions by at least 55% by 2030. In order to achieve cleaner energy, wind energy has become one of many solutions where normally this energy is harvested through wind turbines. The well-known configuration wind turbine is a Horizontal-axis wind turbine or *HAWT*. Plenty of research was done to optimize wind power extraction while minimizing the loading on a wind turbine. Nowadays, commercial wind turbines use a yaw-actuation mechanism to orient the rotor plane to maximize the energy harvest, yet this yield in considerable stress on the joint. To alleviate this solicitation, a free-yaw wind turbine configuration is proposed. A free-yaw wind turbine is stable when it is set in a downwind position which will be discussed further in this paper.

1.2 Dynamic of a downwind free-yaw wind turbine

The Dynamic of a downwind free-yaw wind turbine has been studied since the 1980s. A model for prediction and understanding the yaw behavior was done by the University of Utah and the Solar Energy Research Institute in the US [1]. They depicted that for a downwind free-yaw wind turbine, under vertical wind shear, the wind turbine will align to a steady-state yaw angle thanks to the restorative yawing moment, where it is generated through the lift coefficient profile as the angle-of-attack (*AOA*) of the blade sees through one rotation. More recent research by the University of Southern Denmark and the Technical University of Denmark [2] showed that with the absence of tilt angle and vertical wind shear, the steady state yaw angle will be zero. The simulation that will be done in this master thesis will consider no tilt angle, hence it is useful to mention the finding of the mentioned research.

1.3 Individual Pitch Control (IPC) and Yaw control application

To this date, wind turbines are usually constructed in clustered areas or known as wind farms. Economically it is more beneficial yet this comes with a price of lower power extraction on the downstream wind turbines. Studies were done to mitigate this problem by wake redirection or axial induction control [3]. In this master thesis, the focus will be on wake redirection. This technique can be achieved by applying misalignment between the free-stream flow with the turbine-rotor plane, either by tilt or yaw angle. As mentioned in section 1.2, the tilt angle in this thesis will be zero, hence, this paper will cover the wake redirection due to yaw misalignment. In this master thesis [4], he has shown the results of various strategies of wake redirection.

it is common for HAWT to be equipped with *Individual Pitch Control* (*IPC*). With the help of the IPC, fatigue loading can be reduced [5]. In 2014, Delft University studied for the first time to implement an active yaw control by using IPC numerically. Their study showed that IPC can be used to control the yaw position of an upwind wind turbine and therefore the yaw-actuation mechanism can be removed and lower the structural loads [6]. Nevertheless, the scope of this research is limited to the loading of the structure and the blades, where the power production and the wake downstream are still subjects to be investigated.

1.4 Objectives

To sum up, this master thesis will study the effect of IPC implementation on yaw control. The yaw control architecture is adopted from [6]. The objectives are; 1. To analyze the wake created by the free-yaw wind turbine, 2. To investigate the loads acting on the blades and the structure of the wind turbine, 3. To analyze the power production and the available power at the position downstream. Two different strategies are studied. The first one is where the free-yaw wind turbine is subjected to a static yaw input misalignment. Secondly, the dynamic yaw input is imposed. It is interesting to compare the results with a downwind fix-yaw wind turbine with and without load-alleviating IPC.

Chapter 2

Methodology

In this master's thesis, the simulation is carried out thanks to two simulation tools that are coupled. The first simulation tool is the Vortex Particle-mesh Method (VPM) which solves the flow dynamics. The flow within the domain will generate aerodynamic forces onto the wind turbine. The dynamic behavior of the wind turbine, taking into account the aerodynamic forces, is solved with ROBOTRAN, a multibody solver. In this chapter, the simulation tools and the wind turbine model will be explained.

2.1 Vortex Particle-mesh Method

The flow solver used for the simulations was developed by the collaboration of ETH Zurich and UCLouvain. This variant of vortex methods combines both particle and mesh, exploiting the advantages of both discretizations. The turbulent inflow is modeled in vorticity form. To understand more thorough regarding the methodology of how the flow solver works, the reader is invited to read [7] and [8].

For an incompressible viscous flow Navier-Stokes equations are given by

$$\frac{\partial \mathbf{u}}{\partial t} + (\mathbf{u} \cdot \nabla)\mathbf{u} = -\frac{1}{\rho}\nabla \mathbf{p} + \nu \nabla^2 \mathbf{u} \tag{2.1}$$

$$\nabla \cdot \mathbf{u} = 0 \tag{2.2}$$

where bolded letters are vector entities in 3D space. **u** is the velocity vector and **p** is the pressure term. The vorticity field $\boldsymbol{\omega}$ of a given velocity field in space and time can be written as follow.

$$\boldsymbol{\omega} = \nabla \times \mathbf{u} \tag{2.3}$$

With equation (2.3) the Navier-stokes equation of the momentum conservation can be re-written as in equation (2.4).

$$\frac{\partial \boldsymbol{\omega}}{\partial t} + (\mathbf{u} \cdot \nabla)\boldsymbol{\omega} = \nu \nabla^2 \mathbf{u} + (\boldsymbol{\omega} \cdot \nabla)\mathbf{u} \tag{2.4}$$

The pressure term vanishes knowing that the curl of a divergence will result in a zero field. If one only considers a two-dimensional velocity field, the vorticity will be scalar, orthogonal to the corresponding two-dimensional direction. The vorticity field is discretized with particles which is characterized by a position $\mathbf{x}_p$, a volume V_p and strength $\boldsymbol{\alpha}_p = \int_{V_p} \omega d\mathbf{x}$. The particles are convected by the flow field and their strength is adapted to account for vortex stretching and diffusion. Mathematically these can be expressed as follow.

$$\frac{\mathrm{d}\mathbf{x}_p}{\mathrm{d}t} = \mathbf{u}(\mathbf{x}_p) \tag{2.5}$$

$$\frac{\mathrm{d}\boldsymbol{\alpha}_p}{\mathrm{d}t} = (\nu \nabla^2 \mathbf{u}(\mathbf{x}_p) + (\boldsymbol{\omega} \cdot \nabla)\mathbf{u}(\mathbf{x}_p))V_p \tag{2.6}$$

Thanks to the vorticity and incompressibility constraint, the velocity field is computed by solving the Poisson equation and hence the above particle evolution equations can be calculated [9].

$$\nabla^2 \times \mathbf{u}_\omega = -\nabla \times \boldsymbol{\omega} \tag{2.7}$$

Vortex particle methods are prone to Lagrangian distortion [10] because of weaving particle locations for the discretization of the governing equations. To cope with this problem, it is therefore coupled with a mesh. at uniform time step the particles hence are redistributed over the mesh by interpolating the vorticity from the particles to the node locations. This process helps to compute the different differential operators and solve the Poisson equation in a more efficient manner. For large wind turbines it is common to encounter with high Reynolds number flows where it is normally turbulent and complex. Large Eddy Simulation (LES) will be used to reduce the numerical cost by modeling the small-scale turbulence flow. The Navier-Stokes equations in vorticity form can hence be rewritten into

$$\frac{\partial \boldsymbol{\omega}}{\partial t} + (\mathbf{u} \cdot \nabla)\boldsymbol{\omega} = \nu \nabla^2 \mathbf{u} + (\boldsymbol{\omega} \cdot \nabla)\mathbf{u} + \nabla \cdot \mathbf{T}^M \tag{2.8}$$

The extra term on the right hand sight of equation (2.8) is to express the stress model of the filtered small-scales.

Regarding the time and space discretization, a fourth-order finite difference scheme is used to evaluate the differential operators while a third-order low storage Runge-Kutta scheme is used for the time integration.

The simulations are performed on the Lemaitre3 supercomputer.

2.1.1 Immersed lifting lines

The blades are modelled as a bundle vorticity line. From Helmholtz's theorem, a vorticity line cannot end in the fluid, hence the vorticity line continues as free vortices trailing downstream. These continuing free vortices are known as the vortex sheet or can be seen as vorticity line bundles leaving the blade. The strength of the vorticity lines is quantified by the bound circulation $\boldsymbol{\Gamma}$ around the airfoil and the strength is constant along its length according to Helmholtz's first theorem. From the Kutta-Joukowski theorem, the lift per unit span **L** can be calculated as

$$\mathbf{L} = \rho \mathbf{V}_{\text{rel}} \times \boldsymbol{\Gamma} \tag{2.9}$$

where $\mathbf{V}_{\text{rel}} = \mathbf{u} - \mathbf{u}_{\text{blade}}$ and ρ is the fluid density. The blade profile is discretized in span-wise direction. As the strength of the vorticity and the relative velocity are known, with the airfoil polar data, the aerodynamic performance, namely lift and drag, can be computed.

2.1.2 Turbulent and sheared inflow

The turbulent wind model is generated through Mann's algorithm [11]. The vorticity field of this periodic turbulent flow is evaluated and thereafter it is made compact in boundless directions through a smooth clipping. To transport this turbulent vorticity into the domain vortex particles are created [8].

In this master thesis, only vertical wind shear will will be treated. The shear can be mathematically formulated via the power law as follow

$$\mathbf{U}(y) = \mathrm{U}_0 (\frac{y}{H_{\text{hub}}})^{\alpha} \tag{2.10}$$

and can be written in form of vorticity as

$$\boldsymbol{\omega}(y) = \alpha \frac{\mathbf{U}_0}{H_{\text{hub}}^{\alpha}} y^{\alpha-1} \tag{2.11}$$

Where U_0 is the streamwise velocity at the hub height H_{hub} and α is the shear coefficient.

2.2 Multibody Solver, *Robotran*

In order to solve the multibody system *Robotran* program is used. It is an in-house software at UCLouvain developed by the UCL-MEED research group. In this program, a multibody system is described in a tree-like structure, preventing any loops within itself. For cases of multi-bodies that have one or more loops, a particular procedure will be used to restore a temporary tree-like structure. In this section, the model of the wind turbine will be presented. For the sake of clarity, important remarks about the program will be addressed in the following subsection but further details can be found in [12].

2.2.1 Wind turbine model

In figure 2.1 a tree-like structure of an arbitrary multibody system is presented. A multibody system may consist of several rigid bodies. A body i is characterized by a parent body h and its ”children” bodies j and k. For any joint i, two reference anchor points are defined; firstly, O^i, on the parent body and the second one, O'^i, on the i. At the body center of mass, an orthogonal right-handed body frame $\hat{\mathbf{X}}^i$ is rigidly attached. The body is attached to the child-bodies via joints that are described by vectors pointing from O'^i to O^j. In addition to that, the body is characterized by its mass m^i and $\mathbf{I}^i$ the symmetric inertia tensor of body i with respect to its center of mass CM^i.

In *Robotran*, the joints are assumed to be only free in one degree of freedom, either *prismatic* (denoted in T) or *revolute* (denoted in R). The purpose of this assumption is to prevent the description of a large database of joints. Nevertheless to describe a joint with multiple degrees of freedom, it is possible to model by using intermediate artificial joints (and fictitious massless bodies). To give an example, in figure 2.2 joint number 1 to 6 describes the artificial joints that connect the nacelle to the base of the wind turbine where it the user can measure the yaw position of the nacelle at any given time or to measure different forces (or torque) on a desired position.

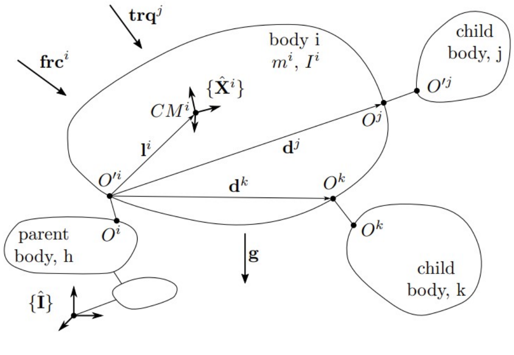

Figure 2.1: Generalized multibody system in *Robotran*

2.2.2 Dynamics of tree-like multibody systems

The equation of motion can be obtained from different multibody formalisms. As mentioned earlier, for a tree-like multibody system, the equations describing the dynamics

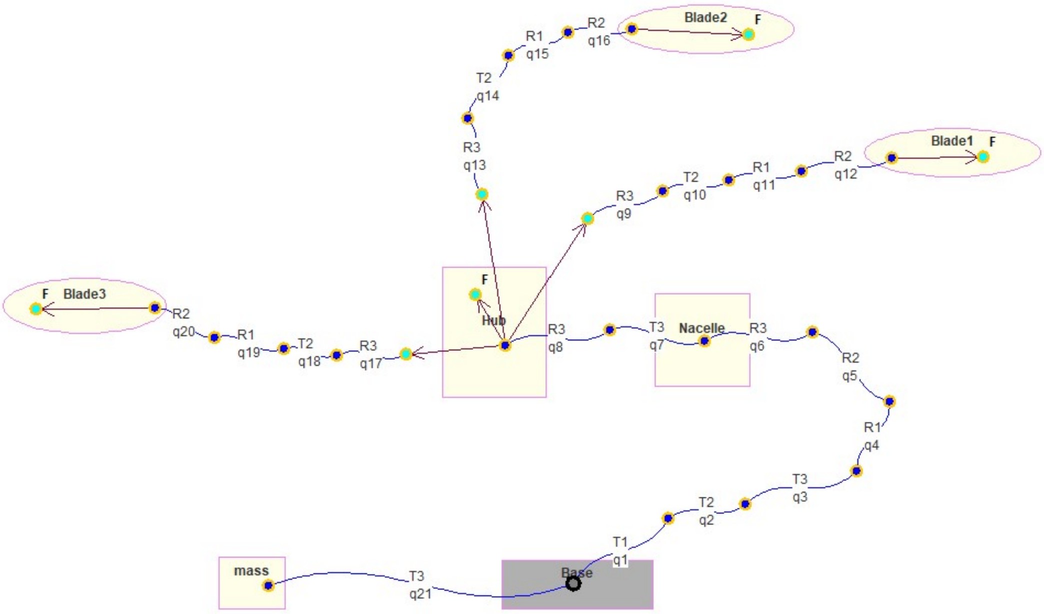

Figure 2.2: NREL5MW multibody tree structure

can be expressed in a *semi-explicit* form in terms of the generalized accelerations [12].

$$M(\mathbf{q},\delta)\ddot{\mathbf{q}} + c(\mathbf{q},\dot{\mathbf{q}},\delta,\mathbf{frc},\mathbf{trq},\mathbf{g}) = \mathbf{Q}(\mathbf{q},\dot{\mathbf{q}}) \tag{2.12}$$

M in equation (2.12) describes the symmetric gerenalized mass matrix of the system, **c** is the non-linear dynamic vector which includes the gyroscopic, centrifugal, gravity terms, and external resultant forces and torques. **q** express the relative generalized coordinates, and **Q** denotes the generalized joint forces (or torques).

equation (2.12) can also be expressed in an implicit manner. In this implicit equation, ϕ is the MBS kinematics and its parameters.

$$\phi(\mathbf{q},\dot{\mathbf{q}},\ddot{\mathbf{q}},\delta,\mathbf{frc},\mathbf{trq},\mathbf{g}) = \mathbf{Q}(\mathbf{q},\dot{\mathbf{q}}) \tag{2.13}$$

2.3 Coupling of Vortex Particle-mesh Method and multibody system solver

The detail of the coupling is explained in [13] yet it is important to understand the overview of the coupling between the two solver. The flow solver and the multibody sytem solver are ran independently, however a weak coupling is implemented which connects the two solver during synchronization steps. The flow solver is the *master* between this coupling as it requires more computational cost and hence the ROBOTRAN is the *slave*. At a given time t, the flow solver evaluates the aerodynamic forces. This information is then passed to ROBOTRAN that evaluates the position $\mathbf{q}$ and velocities $\dot{\mathbf{q}}$ component of the lifting lines. Knowing these two variables, the flow solver shed the vortices accordingly in the flow domain.

2.4 Wind turbine parameters and associated controllers

The wind turbine model used in this master thesis is NREL5MW. This type of wind turbine is commonly used for offshore wind farms. The parameters of this wind turbine can be found in table 2.1. The wind turbine's control system is related to the working region of itself. In figure 2.2 the power production as a function of various wind speeds is depicted for an arbitrary wind turbine. The purpose of presenting this figure is to let the reader understand the general overview of a wind turbine's working principles at various wind speeds. The measurement starts at 4m/s where this is considered as the *cut-in* speed. Below this speed, the wind turbine will still rotate yet there is no power production as it is not coupled with the generator. When the wind velocity is high enough (in this case above 11 m/s), the power production is maintained constant by varying the blade's pitch angle. This threshold wind speed is considered as the *rated wind speed* and above a certain wind speed (in this case 25m/s) is the *cut-out wind speed* where the purpose is to prevent unwanted damage to the wind turbine. Between the cut-in speed and the rated wind speed, the wind turbine rotor speed is maintained such that it achieves the optimum tip-speed ratio (optimum TSR).

Column 1	Column 2
Rated power	5MW
Rotor and hub diameter	126m, 3m
Hub height	90m
Cut-in, rated and cut-out wind speed	3m/s, 11.4m/s, 25m/s
Cut-in and rated rotor speed	6.9rpm, 12.1 rpm
Optimal tip-speed ratio (Optimal TSR)	7.55

Table 2.1: NREL5MW Dimension and Parameters.

The control system in this master thesis can be categorized into three parts, namely the *Generator-torque controller*, *Collective blade-pitch controller* (CPC), and *Individual pitch controller* (IPC). To achieve maximum power production under the rated wind speed, the generator-torque controller is used in a manner as explained previously. Above the rated wind speed the collective blade-pitch controller is armed to maintain power production. These 2 main controllers are normally called the *baseline controller*.

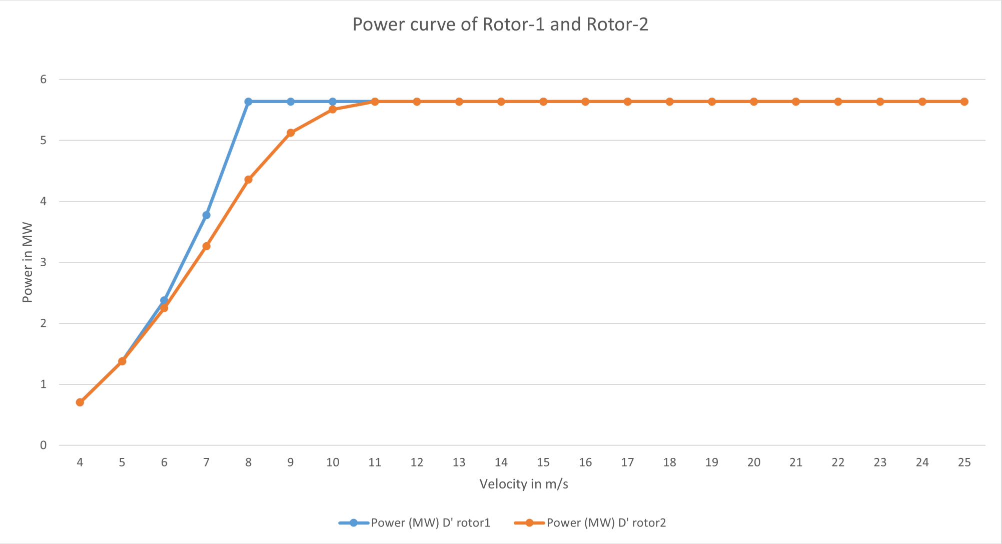

Figure 2.3: Power Curve of an Arbitrary Wind Turbine

It is very likely that modern commercial wind turbines to implement the baseline. As has been briefly mentioned in the introduction, the last part of the controller is the *individual-pitch controller* or *IPC* which is usually used to alleviate the blade loading. As the name describes itself, individual blades are equipped with actuators to change the pitch angle and are normally located at the hub. The controller architecture of a load-alleviating IPC is depicted in figure 2.4.

For the sake of clarity, for a load-alleviating IPC, the *yaw angle* path can be disregarded at the moment and the baseline controller is not included in this controller scheme. the wind turbine provides the blade-wise bending moment which is orthogonal to the direction of the incoming wind, from all three blades. Thanks to *Coleman transform* the blade-wise bending moments are projected into two orthogonal directions which are; the tilting moment and the yawing moment. With the PI controller, the desired input of the tilt and yawing moment is set to zero, and finally, each blade pitch angle is calculated by using the *inverse Coleman transform*.

As has been mentioned in the introduction, the motivation of this master thesis is to remove the yaw actuator. Now, the entire control architecture in figure 2.4 is considered. The architecture of this control scheme is first introduced by [6] and will be used in this master thesis. The wind turbine yaw position is returned by the wind turbine. The difference between the desired yaw position between the current yaw position is calculated and is considered as yaw error. The yaw error is then passed to a saturation box to allow small misalignment. In this master thesis, the yaw error is relaxed to one degree. with the PI controller, the input is then added to the yaw controller before it is passed to the inverse Coleman transform. From this point onwards, the yaw control will be called as *yaw-IPC*, and to prevent misunderstanding between yaw-IPC and the yaw component of the load-alleviating IPC, *yaw-load-IPC* will be used to point the load-alleviating yaw-moment control.

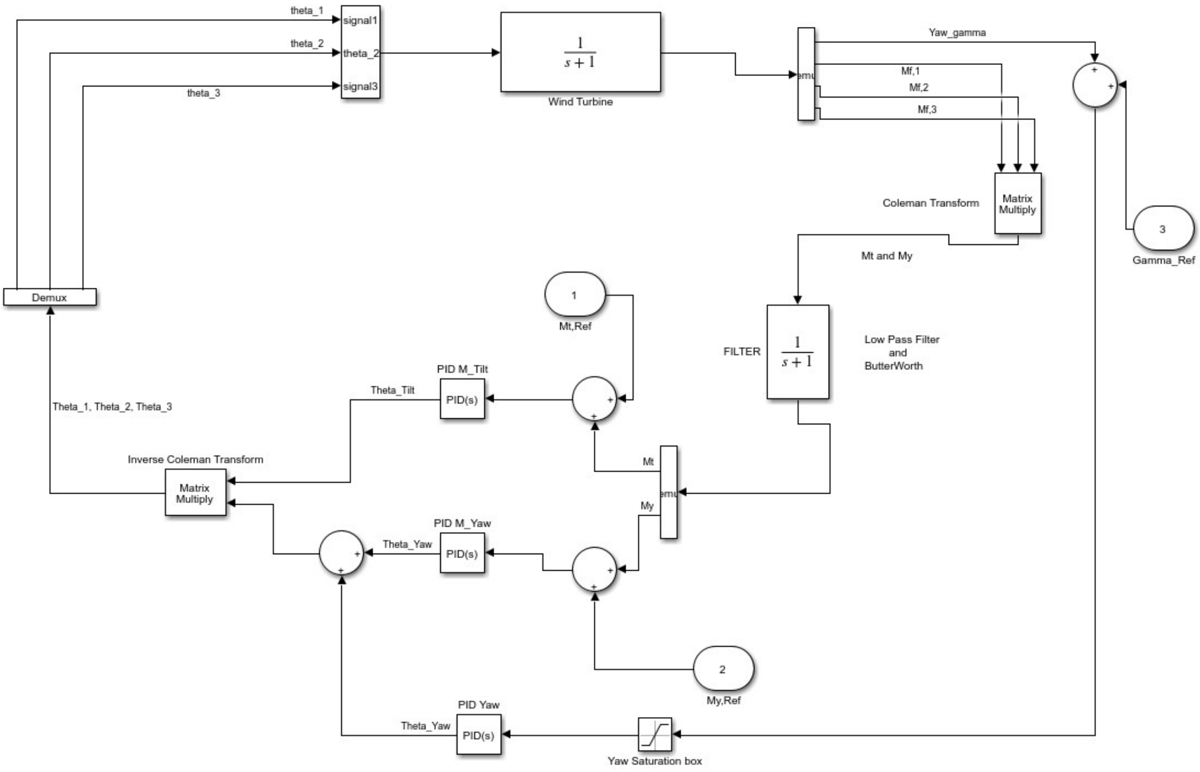

Figure 2.4: Individual pitch control for load and yaw control

2.5 Analyses methodology

First, the methodology to evaluate the damage equivalent loading will be presented. Following that the methodology to track the wake center and the methodology to evaluate the available power be discussed. The methodology on wake tracking is based on the master thesis of N.Coudou [14] whereas the fatigue loading is evaluated with Damage Equivalent Loading (DEL) [15] and relies on *rainflow* counting. Each method will be briefly explained. Finally, the numerical setup of the simulations will be presented.

2.5.1 Damage Equvalent Loading (DEL)

The fatigue loading quantification is evaluated by using *Damage Equivalent Loading* (DEL). This approach adopts Miner's linear damage principle which does not presume that any information about the materials or blade structural properties is precisely known. Normally it is depicted as *stress-cycle* (S-N) curves. The DEL method, however, converts the moment loading into a family of M-N curves (moment vs cycles).

By using *rainflow* counting, a loading sample is grouped into different fatigue cycles of different amplitudes. Afterward the equivalent fatigue loading M_{eq} can be calculated by using equation (2.14). n_i refers to the number of cycles of amplitude $M_{a,i}$, n_c is the number of amplitude bins that are used to group the different fatigue cycle of different amplitudes, N_{eq} is the total amount of cycle of each different magnitude, and m is the fatigue slope of an M-N (or S-N) curves.

$$M_{eq} = (\sum_{i=0}^{n_c} \frac{n_i M_{a,i}^m}{N_{eq}})^{(\frac{1}{m})} \tag{2.14}$$

2.5.2 Wake tracking

In the PhD thesis of N.Coudou [14], Wake tracking is done for a 3-Dimensional velocity field by a convolution between the power density and a spatial Gaussian function. He also proposed a methodology to track the wake centroid in a horizontal plane, which is used in this master thesis.

First, the velocity field at hub height is extracted at an arbitrary time snapshot. The power density in that field is then calculated as follows.

$$p = \frac{1}{2} u_z |\mathbf{u}|^2 \tag{2.15}$$

where $\mathbf{u} = \sqrt{{u_x}^2 + {u_y}^2 + {u_z}^2}$

Thereafter, the power density is convoluted with a 2-Dimensional spatial Gaussian function which is expressed in the equation (2.16), where $A = -1$ and $\sigma_x = \sigma_z = D/4$

$$f_{G,2D_{hp}}(x,z) = A \, \text{exp}(-(\frac{x^2}{2\sigma_x^2} + \frac{z^2}{2\sigma_z^2})) \tag{2.16}$$

Finally, the wake centroid, x_c, can be located from the maximum of the convolution field for each downstream position.

$$x_c = \text{argmax}(p * f_{G,2D_{hp}}) \tag{2.17}$$

The figure shows the u_z velocity field and the wake centroid is tracked. It can be seen behind the rotor position, a high-velocity field occurred as the hub and the nacelle are not modeled, resulting in wake tracking errors for 0D to 2D downstream position. This occurrence is also observed in [4] and [14]. Therefore, the downstream wake characteristic is evaluated starting from the 3D downstream position.

With the wake centroid information, the wake meandering amplitudes and waves can be calculated. The methodology is the same as proposed from [14]. The wake centroids is low-pass filtered spatially with cut-off length $L_{\text{cut-off}} =$ 1D. The amplitude of wake meandering is measured as half the cross-wind distance between consecutive

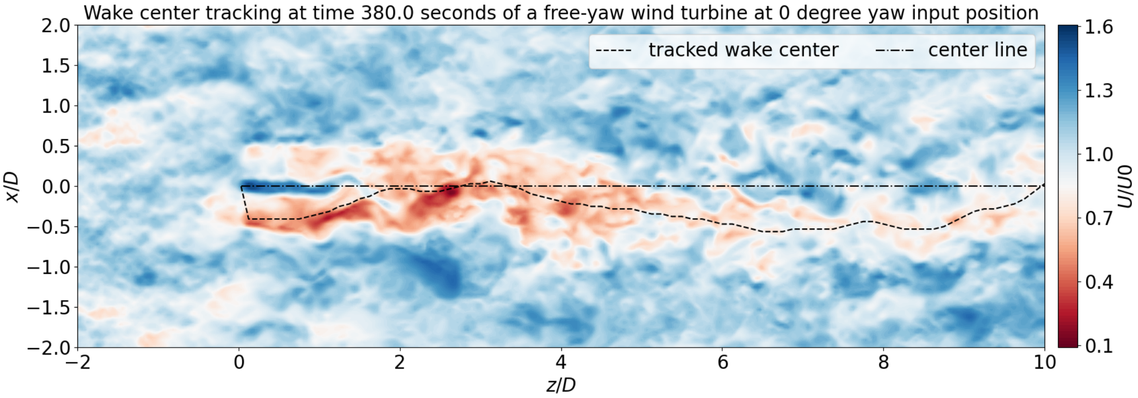

Figure 2.5: Wake centroid tracking at time 380.0 second of a free yaw wind turbine at $0°$ yaw input position

maximum-minimum of the filtered centroids. The wavelength is measured between two consecutive maxima or minima in the streamwise direction. The quantities were binned, with respect to the downwind distance from the rotor. The bin size is set to half-diameter of the rotor and the mean values are then computed. To give a better visualization of the amplitude and the wavelength, figure 2.6 is presented.

2.5.3 Available power downstream

Available power downstream is the available power that can be harnessed by a wind turbine that is located at the downstream position. figure 2.7 shows the z-slices (or-

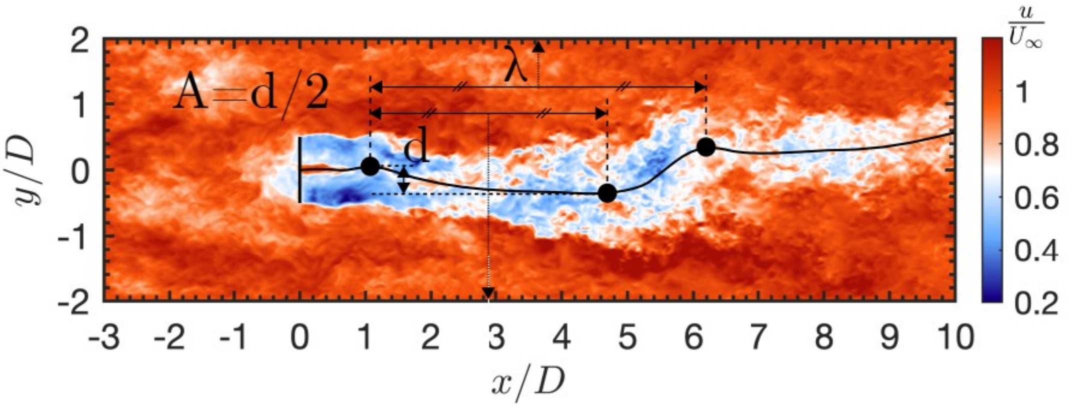

Figure 2.6: Schematic of the amplitude and wavelength definition [14].

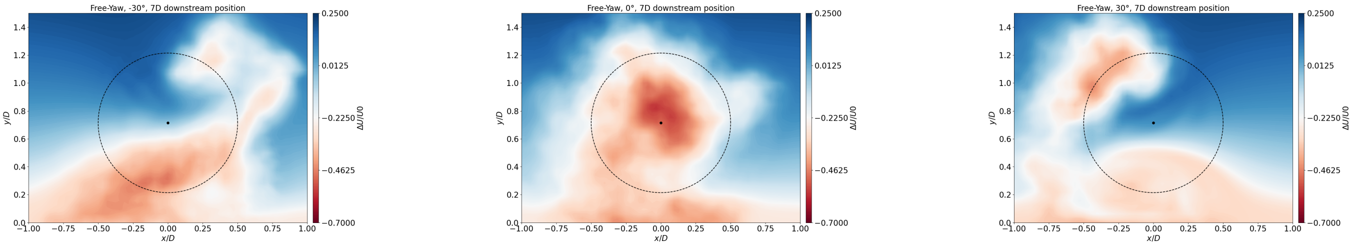

Figure 2.7: Mean stream-wise velocity deficit at -30°, 0°, and 30° yaw input position (from left to right) of a free-yaw with load-alleviating and yaw-IPC at 7D position downstream.

thogonal plane to the free-stream direction) of the mean stream-wise velocity deficit, looking from downstream to upstream. The circle is the projection of the rotor surface of a hypothetical wind turbine that is located at a downstream position. The center of the circle is aligned with the center of the upstream wind turbine. The hypothetical wind turbine has no yaw misalignment. The available power is calculated from the sum of the encircled stream-wise velocity.

2.5.4 Numerical setup

The simulations are ran using the *VPM* code and *Robotran* as the multibody solver. Two different strategies will be studied; static yaw input misalignment and dynamic yaw input misalignment. As depicted in figure 2.2 the bodies are taken into account namely; the nacelle, the hub, and the three blades, however, only the blades are modeled with immersed lifting lines. To prevent misunderstanding on the direction, the coordinate system that is used is depicted in figure 2.8. The flow direction is pointing in the positive z-direction, the positive y-direction pointing upwards, and the positive x-direction follows the right-hand rule. The simulation domain is shown in figure 2.8 where it is composed with a size of 12D $\times$ 4D $\times$ 3D with a resolution of 32 points per diameter. The wind turbine is located 2D downstream of the domain entry and the center of the wind turbine is aligned to the mid-length of the lateral domain size (0D). The free-stream velocity $\mathbf{U}_0$ is set to 9.5m/s normal to the x-y plane at the hub height, hence, the turbine working region is below the rated wind speed. The shear flow coefficient is set to 0.2 (see equation (2.10)) and the turbulence intensity is 10%, synthesized with a Mann box [11] that is 32-diameters long. The flow is studied after 16 convective times (4/3 of the length of the domain). For the static yaw input misalignment strategy, two cases will be considered, which are with and without turbulence. For the free-yaw case, the wind turbine is set free from the beginning of the simulation to prevent the influence of the fix-yaw wake that develops before the measurement. The yaw-IPC is started at

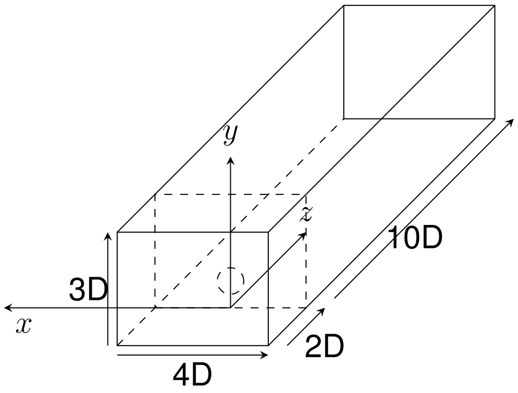

Figure 2.8: Domain of the simulation (drawing is not to scale)

16 convective times. Two regions can be defined for the free-yaw wind turbine namely the transient and the steady state period. The transient period is when the wind turbine started to move to the desired position, and the steady state period is when the yaw turbine remains stationary. The purpose to separate these two periods is to understand how the wind turbine redirects itself to the desired position, and the steady state period is to study the wake characteristics and the blade fatigue loading. The transient period considers 4 convective times after the yaw-IPC is started, while the steady state is studied for a period of 12 convective times from the end of the simulation. For the turbulence case, the measurement duration is one through-flow of the Mann-box size (32D) convective times. Three wind turbine setups are considered in this study; Fix-yaw without load-alleviating IPC as the control, Fix-yaw with load-alleviating IPC, and Free-yaw with load-alleviating and yaw IPC. Each case is studied with different yaw input positions, starting from -30° to 30° with 15° step, totaling 15 cases. In the dynamic yaw input misalignment strategy, only the turbulence case is considered. The free-yaw wind turbine is subjected to dynamic yaw misalignment input, with the amplitude and frequency that will be discussed in chapter 4. The dynamic yaw input misalignment will be compared to the static yaw input misalignment of the fix-yaw and free-yaw wind turbines. More details will be explained in chapter 4.

Chapter 3

Static yaw input misalignment

In this chapter, the static yaw input misalignment will be studied. The purpose of this is to redirect the wake and allow the potential downstream wind turbine to increase its power capture. The wind turbine is subjected to the wind shear and two different are considered; with and without turbulence. In [4], the loading and the wake characteristic have been analyzed for an upwind and downwind fix-yaw wind turbine at various yaw positions. This master thesis validates the cases that are shown in [4] and an additional case is added where the yaw mechanism of the wind turbine is controlled by the loads acting on the blade.

3.1 Shear flow without turbulence

Figure 3.1 depicts the yaw position of the wind turbine and the corresponding yaw rotational speed. As stated before the load-alleviating and yaw-IPC are started at 16 convective times. The yaw-IPC moves the yaw position of the wind turbine and stabilizes after 20 convective times. The transient period starts from 16 convective times to 20 convective times, while the steady-state period begins from 20 convective times. The wind turbine yaw position does not stabilize at the desired yaw position and creates a static yaw error. This will be discussed further in subsection 3.1.2. The yaw rate contains an oscillatory behavior due to the 3P frequency (3 times per revolution). The mechanism to redirect the yaw position by using the blade loading is analyzed in subsection 3.1.1. In the steady-state period, the stability of the yaw, the load that acts on the wind turbine, and the wake profile will be discussed.

3.1.1 Transient period

Figure 3.2 shows the instantaneous flap-wise bending moment of different input yaw positions, as a function of its azimuthal position. Looking from the downstream position,

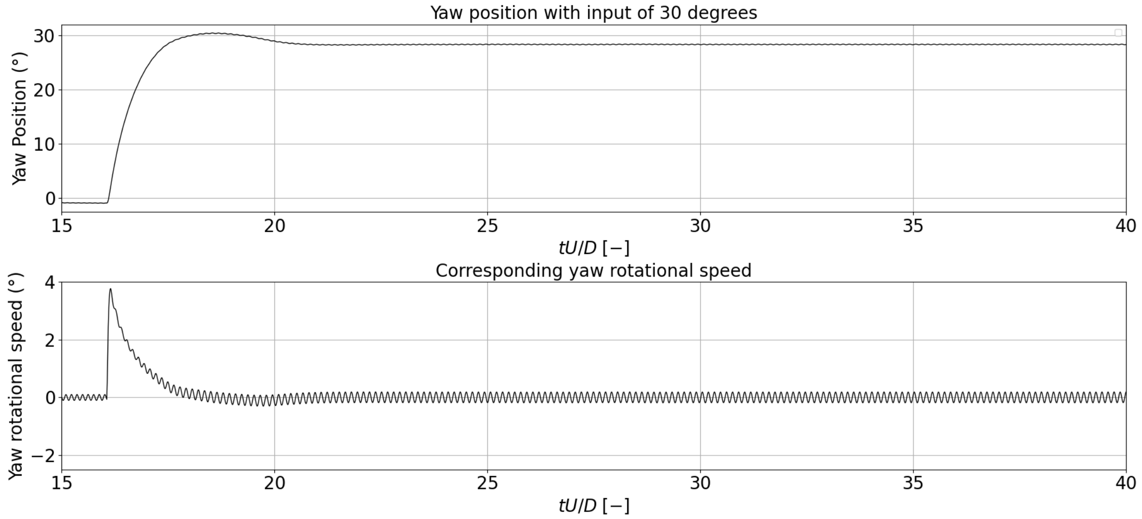

Figure 3.1: Yaw position evolution (top) and the corresponding yaw rotational speed (bottom).

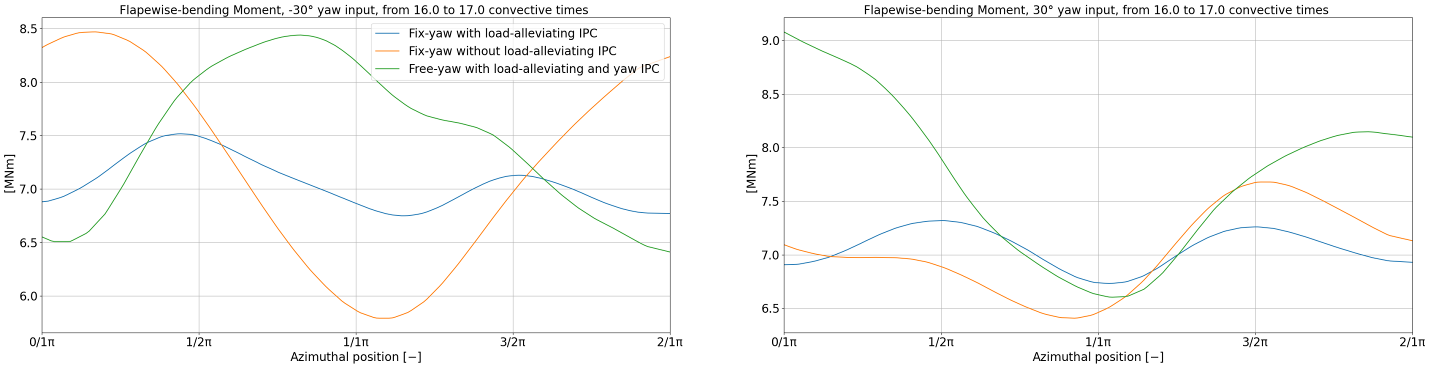

Figure 3.2: The instantaneous flap-wise bending moment after the load-alleviating and yaw-IPC are started at time convective equal to 16 (left) measured for one period of convective times. Yaw input is set to -30° (left) and 30° (right)

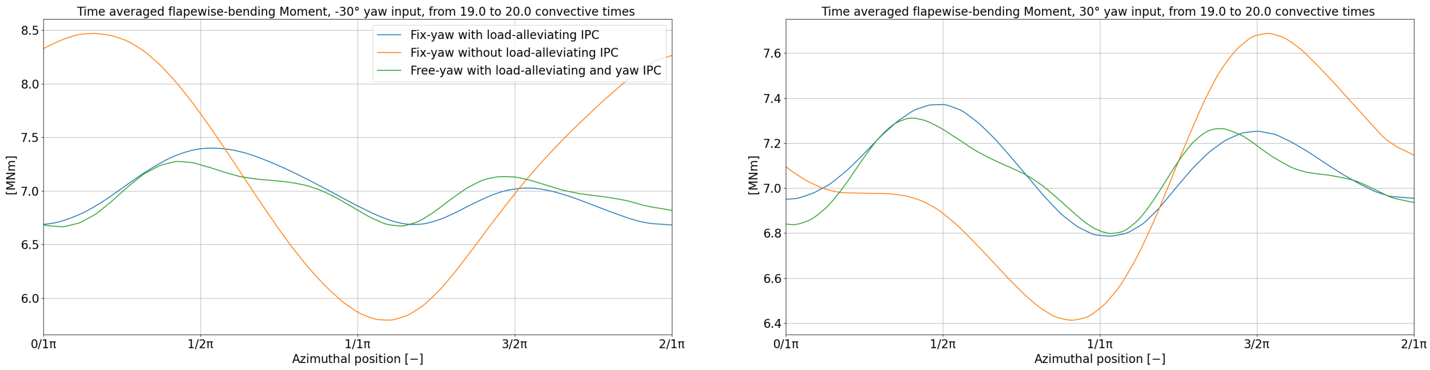

Figure 3.3: The instantaneous flap-wise bending moment at time convective equal to 19 (left) measured for one period of convective times. Yaw input is set to -30° (left) and 30° (right)

the azimuthal position is zero when the blade is pointing to the positive y-direction, and it increases in the counter-clockwise direction. The instantaneous flap-wise bending moment is measured for one convective time period right after the load and yaw-IPC are started. Due to the wind shear, the flap-wise bending moment of the fix-yaw without load-IPC shows a higher magnitude at 0 azimuthal position than in π azimuthal position. By misaligning the wind turbine to the positive yaw position, the flap-wise bending moment at 0 azimuthal position is reduced as the blade sees a lower relative velocity, while it rises the flap-wise bending moment at π azimuthal position due to higher relative velocity seen by the blade. Negative yaw misalignment does the opposite. The load-IPC mitigates these load imbalances by changing the pitch angle of the blade. [4] showed a similar flap-wise bending moment of the fix-yaw wind turbine profile. The instantaneous flap-wise bending moment of the free-yaw wind turbine is the interest in this section. When the input yaw position is set to -30° it shows a significantly higher magnitude at the proximity of azimuthal position equals to π than at azimuthal position equals to 0, on the contrary, the opposite profile is shown when the yaw input is set to 30°. Thanks to this difference in the flap-wise bending moment it helps the wind turbine to steer itself.

Figure 3.4 shows the schematic of a free-yaw wind turbine. The left part of this figure shows the side view of the wind turbine. The wind turbine's nacelle is allowed to yaw freely and rotates along the y-axis. It is then connected to the hub, where the blades are attached, which rotates around the z-axis. The rotation of the hub has angular momentum that points downstream. A change in angular momentum direction needs to be created to yaw the wind turbine. By using equation (3.1), the change in the angular momentum direction can be created by creating torque in the correct direction. Consider the case where the yaw input position is set to 30°. The difference between the flap-wise bending moment at 0 and π azimuthal position creates a torque pointing

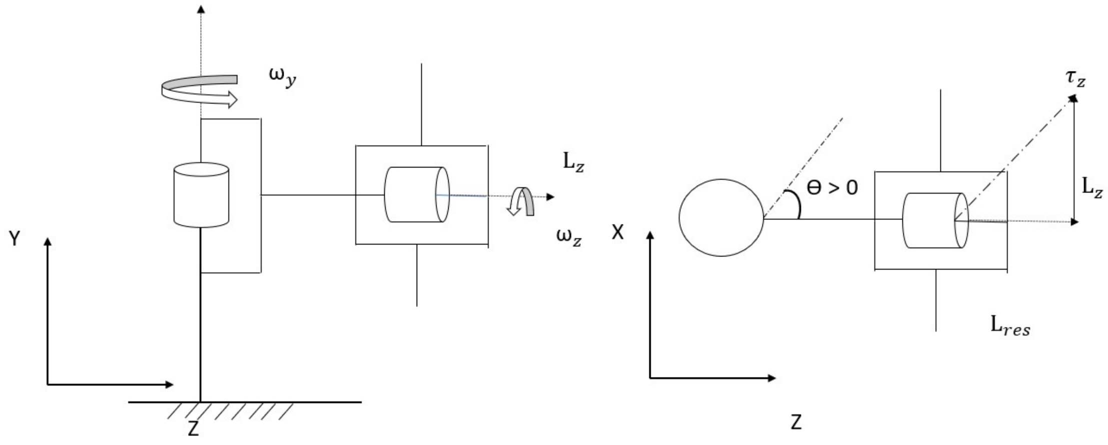

Figure 3.4: Schematic of a free-yaw wind turbine from side view (left) and top view (right).

to the positive x-direction (into the paper). This torque induces a change in angular momentum direction, resulting in a net angular momentum where it is composed with the desired direction of the yaw. The wind turbine hence rotates to the positive yaw position thanks to the net angular momentum. The same argument is also true for the opposite case. As time increases, the difference between the flap-wise bending moment at the proximity of 0 and π azimuthal position shrinks as it yaws closer to the desired yaw position as shown in figure 3.3.

$$\frac{d\vec{L}}{dt} = \vec{\tau} \tag{3.1}$$

3.1.2 Steady state period

Figure 3.5 depicts the stability of the yaw-IPC of the wind turbine. When a free-yaw wind turbine is not controlled by the load-alleviating nor the yaw-IPC, the wind turbine tends to rotate to a steady state yaw position which is close to $0°$ as depicted in figure 3.1 before the load and yaw-IPC is turned on. This is due to the restoring yaw moment where the restoring yaw moment is positive when the wind turbine is negatively misaligned and vice versa [1]. The yaw error measures the difference between the instantaneous yaw position to the input yaw position. The mean yaw error is calculated by taking the yaw error absolute value and is averaged throughout the aforementioned period of measurement. The further the yaw input position is, the bigger the mean yaw error becomes. The standard deviation of the yaw error has the same profile as the mean yaw error, however, the standard deviation is negligible compared to the mean yaw error.

Wind farms normally locate the downstream wind turbine at the far-wake region,

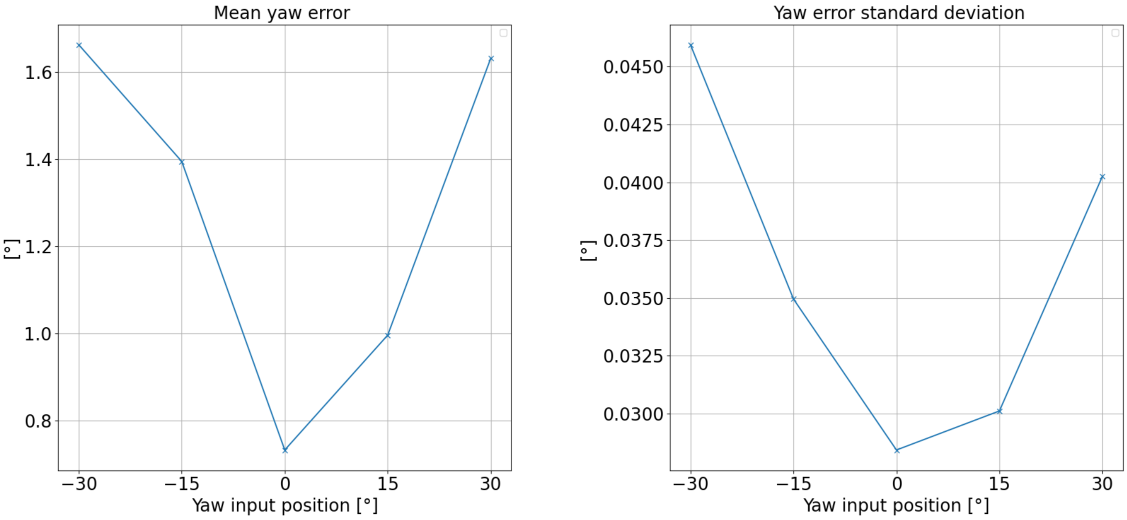

Figure 3.5: Yaw error mean and yaw error standard deviation for a free-yaw wind turbine at various input yaw angle

in the hope that the wake has recovered and thus the wake deficit from the upstream wind turbine does not lower the power harnessing. It is interesting to see the far-wake produced by the free-yaw wind turbine when it is misaligned with the yaw-IPC. The mean wake center position at 6D, 7D, and 8D are calculated along with its standard deviation (figure 3.6). The contribution of the mean yaw error is insignificant toward the mean wake center position, as it shows agreement when the yaw input position is set from -15° to 30°. However, the mean wake center position deviates at -30° yaw input position for the fix-yaw with load-IPC and the free-yaw wind turbine. The fix-yaw without load-IPC showed an increment in the mean wake center position as it measured further downstream, while the standard deviation remained close to zero. On the other hand, the fix-yaw with load-IPC and the free-yaw wind turbine show a slight increase in their standard deviation. Despite the inaccuracy, other measurements show agreement. This agrees with the finding of [16] where the wake characteristic varies slightly from different wind turbine setups as it is less influenced by the detailed features of the wind turbine.

Figure 3.9 shows the power production, the flap-wise bending moment calculated with DEL method, and the available power downstream. The fix-yaw wind turbine without load-IPC is the reference case in the calculation. The yaw misalignment causes less power production as the wind turbine is not aligned with the incoming wind turbine. The wind turbine, which is equipped with the load-IPC, harnesses less power than the fix-yaw wind turbine without load-IPC in most cases. The load-IPC deviates the angle of attack of the blades from the optimum induction factor, causing less power production.

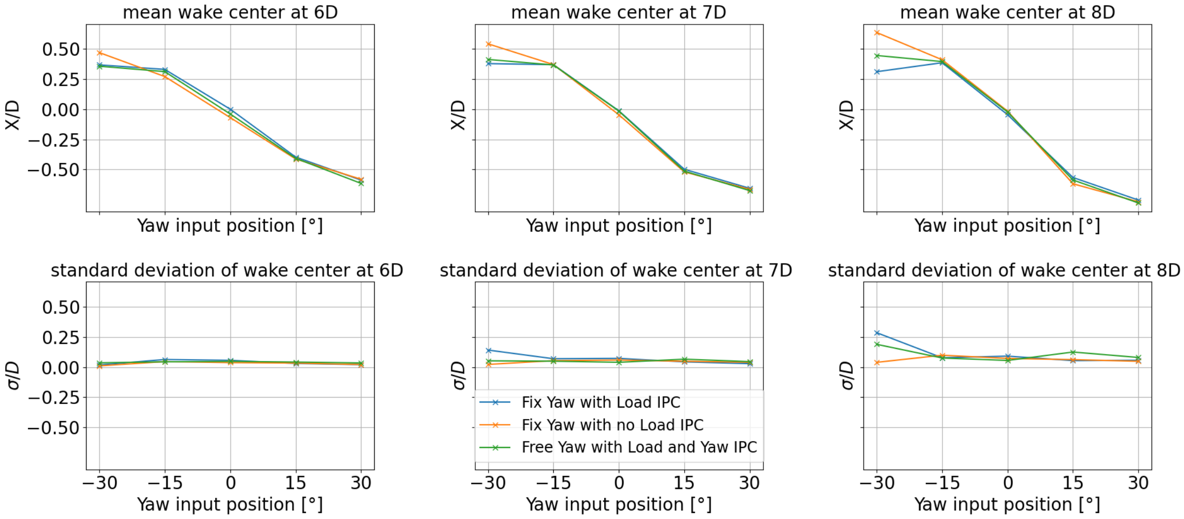

Figure 3.6: mean wake center position (top) and standard deviation (bottom) at 6D,7D, and 8D (from left to right) downwind location from the rotor

In the case of -30° to 15° yaw misalignment, the power produced by the free-yaw wind turbine is higher than the fix-yaw with load-IPC, and it is higher than all the fix-yaw wind turbine when it is misaligned to 30°. The difference in the power production between the free-yaw wind turbine with the fix-yaw wind turbine with load-IPC is increased as the yaw misalignment diverges from 0° yaw position. This relative difference appears to grow with the mean yaw error of the free-yaw wind turbine. The relative difference in the power production of the fix-yaw wind turbine agrees with what [4] found.

The load-IPC attenuates the DEL of the flap-wise bending moment. In general, it reduces the loading imbalance of the flap-wise bending moment. Before going into the DEL of the flap-wise bending moment, one should understand how the load-IPC acts on the flap-wise bending moment cyclic load. Consider the case where the yaw is set to -30° position in figure 3.7. With respect to the fix-yaw wind turbine without load-IPC, the load-IPC decreases the loading at 0 azimuthal position and increases the flap-wise bending moment when the blade is at π azimuthal position. Therefore the loading imbalance is decreased. The profile of the blade-wise bending moment cycle between the free-yaw and the fix-yaw with load-IPC appears to be similar, yet, the average seems to rise for the free-yaw wind turbine when the yaw misalignment is increased. The DEL of the flap-wise bending moment load of the fix-yaw wind turbine without load-IPC decreases as the yaw moves to a positive yaw position. This is because the positive yaw misalignment reduces the loading imbalances as has been described earlier. The free-yaw wind turbine flap-wise bending load increases as the yaw misalignment moves further from 0° yaw position and appears to be symmetrical.

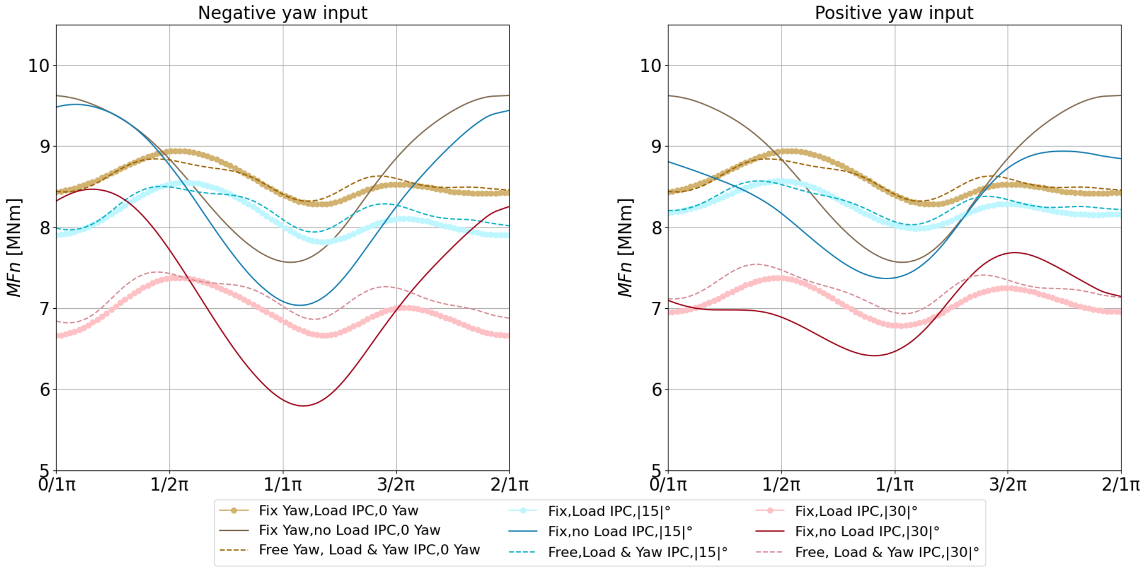

Figure 3.7: Time-averaged flap-wise bending moment, measured from 28 to 40 convective times

This can be related to the fact that the free-yaw wind turbine has to counteract the restoring yawing moment when it is misaligned (see figure 3.8).

As explained earlier, the yaw misalignment redirects the mean wake center position. The redirected wake allows a higher wind velocity at the center line of the lateral position and reduces the wake deficit. Figure 2.7 shows the time-averaged wake deficit at 7D position downstream and the circle represents an imaginary rotor surface of a wind turbine located at the same z-axis. The wake deficit dictates the power available that can be harnessed by a wind turbine that is located at the center line position. The effect of the yaw misalignment on the available power downstream can be seen in figure 3.9. In most cases, the power available downstream is relatively similar except when the wind turbine yaw is set to -30°. It shows that the power available difference is noticeable between the wind turbine with load-IPC and without the load-IPC.

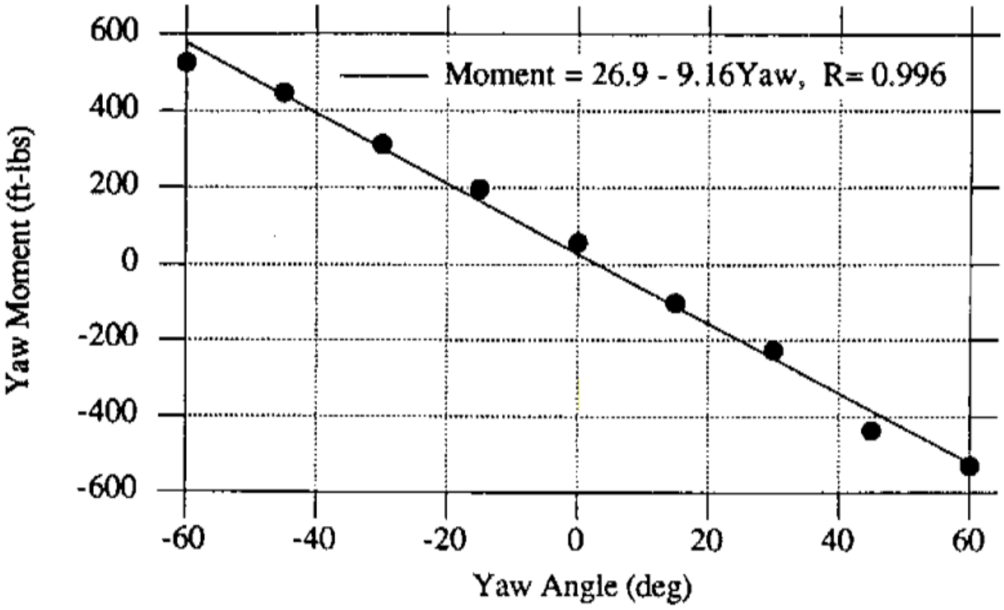

Figure 3.8: Variation of the predicted mean yaw moment of a free-yaw wind turbine. Measured with no turbulence, with vertical wind shear, and wind speed of 37 ft/s [1].

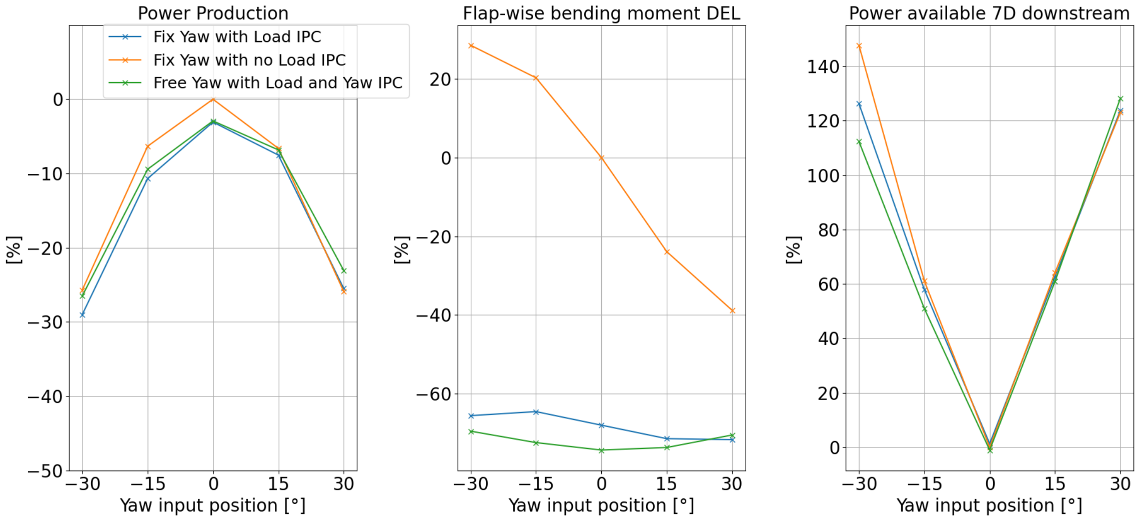

Figure 3.9: Power production (left), Flap-wise bending moment (center), and power available at 7D downstream location from the wind turbine (right), at different input yaw positions and different wind turbine configurations.

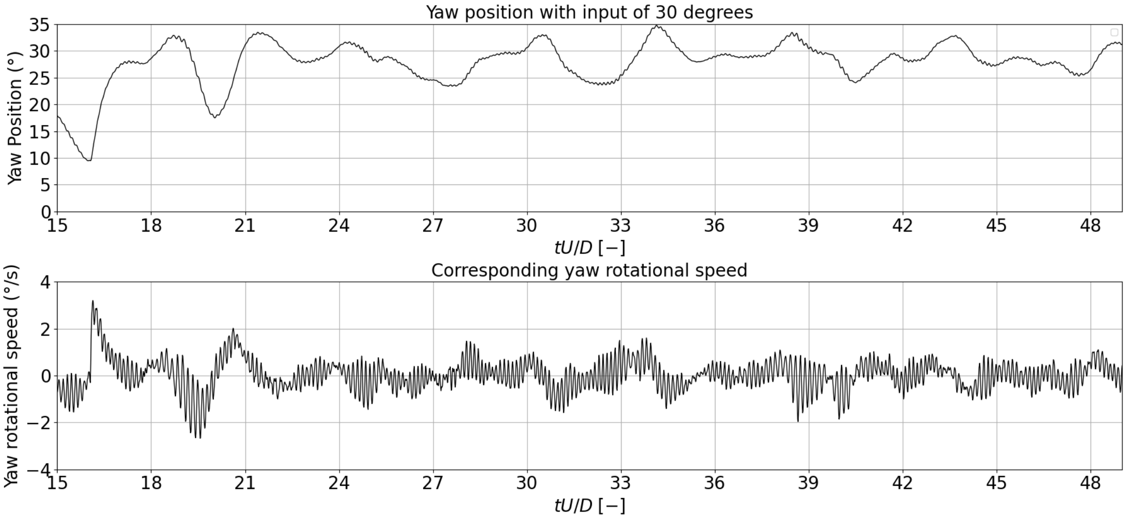

Figure 3.10: Yaw position evolution (top) and the corresponding yaw rotational speed (bottom) when imposed with turbulence.

3.2 Shear flow with turbulence

This section gives a more realistic working wind turbine condition when turbulence is incorporated into the simulation. The yaw position and the yaw rate when exposed to turbulence are shown in figure 3.10 along with the mean yaw error and yaw error standard deviation. In figure 3.11, it is obvious that due to the turbulence, the yaw-IPC cannot maintain steadily the desired yaw position. The yaw rate is unfiltered and it is relatively high in comparison to the yaw rate of a yaw actuator mechanism which is around 0.3°/s. [17] has investigated where the yaw rates reached up to $5^\circ/s$, hence the presented yaw rate in this simulation is acceptable. The difference between the maximum and the minimum mean yaw error deviates slightly to around 0.13°, while the difference of the yaw error standard deviation span to 0.4°. The yaw error standard deviation grows as the yaw misalignment goes up. With respect to the no-turbulence case, the yaw error standard deviation is more impacted by a considerable increase. The increase in the mean yaw error is inferior to the increase in the yaw error standard deviation. With the same controller architecture [6] has shown a yaw error standard deviation up to 13.97° when exposed to a turbulence intensity of 14%.

Figure 3.12 displays the mean wake center position and its standard deviation from 6D to 8D distance downstream from the wind turbine. At zero and negative yaw misalignment input positions, it is clear that the mean wake center position is shifted downwards for the free-yaw wind turbine. For the positive yaw input misalignment, only the 15° yaw input position shows in accordance with the fix-yaw wind turbine, yet it starts to

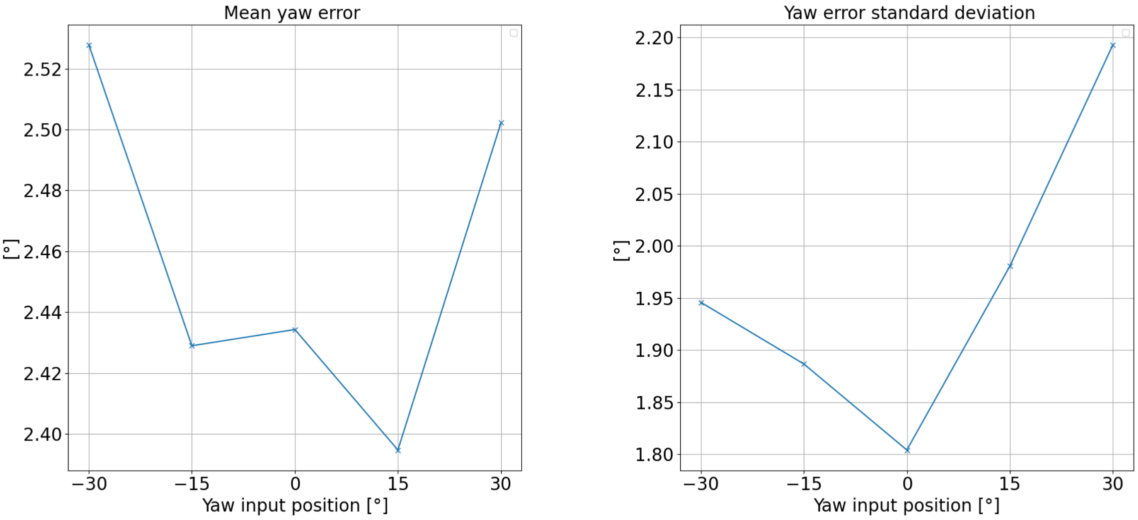

Figure 3.11: Yaw error mean and yaw error standard deviation for a free-yaw wind turbine at various input yaw angles with turbulence.

show a minor deviation at 7D and 8D. At the extreme positive yaw input position (which is 30° in this case), the mean wake center position moves towards the center line. The observations mentioned above are caused by the mean yaw error.

The wake-meandering amplitudes and wavelengths are shown in figure 3.13. Looking at the amplitudes, the magnitude increases as it moves further downstream except for the fix-yaw wind turbine without the load-IPC at 0° yaw input misalignment. The wavelengths are stable within 4D to 8D positions and decrease afterward. The magnitude of the amplitudes corresponds to what has been found by [14]. On the other hand, the magnitude of the wavelengths is slightly lower. The increase of the amplitudes has also been observed by [14], [4], [18], and [19] and it is evident that the growth of the amplitude is approximately linear with the downstream position (z-direction) [20]. Nevertheless, the slope of the growth of the amplitude increases as the yaw input misalignment is increased. This corresponds to [4] observation. At the same given magnitude of yaw input misalignment (either positive or negative), the far-wake characteristics of the free-yaw wind turbine do not show any significant difference in comparison to the fix-yaw wind turbine wake characteristic. Except for -30° yaw input misalignment, the growth of the magnitude of the amplitude of the free-yaw wind turbine is marginally smaller than the fix-yaw wind turbine with the same input yaw misalignment. The yaw error is inconsequential toward the wake meandering. This is also supported by [21] findings where the far-wake region is less influenced by detailed features of the wind turbine, yet, universal characteristics, such as; incoming flow conditions, and global wind-turbine parameters affect more. When moving downstream, and with the largest

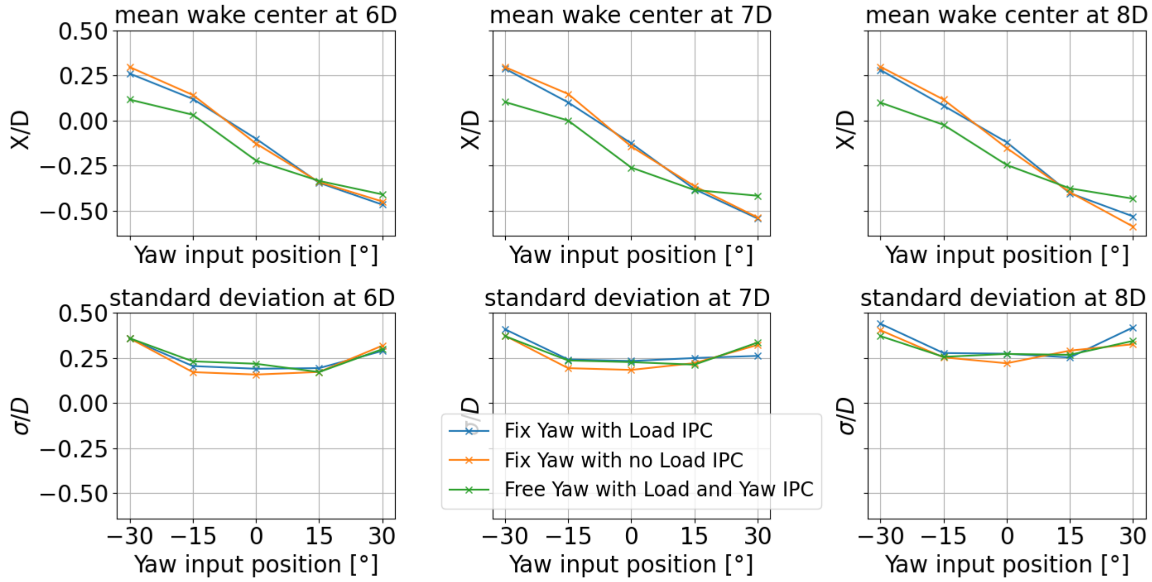

Figure 3.12: mean wake center position (top) and standard deviation (bottom) at 6D,7D, and 8D (from left to right) downwind location from the rotor, with turbulence.

yaw input misalignment, the amplitude of the meandering shows a significant difference. In terms of magnitude, the negative yaw input misalignment shows a bigger amplitude than the positive yaw input misalignment, except for the case of the free-yaw wind turbine that has been mentioned earlier. This phenomenon is also observed by [4].

The mean velocity profile at 6D to 8D downstream position at ±30° and ±15° are presented in figure 3.14. Figure 3.14b shows the yaw input misalignment of ±15°. The free-yaw wind turbine with negative yaw input shows a shift of the wake velocity deficit extrema position closer to the center line and becomes more apparent when measured at different positions downstream. The wake velocity deficit position of the fix-yaw wind turbine (with and without load-IPC) moves away from the center line as the downstream position increases. This shift in the wake deficit extrema position is due to the mean wake center position (see figure 3.12). On the other hand, the wake velocity deficit position of the free-yaw wind turbine with positive yaw input misalignment varies slightly from the wake velocity deficit position of the fix-yaw wind turbine. The effect of the mean wake center position is more conspicuous in figure 3.14a for both positive and negative yaw input misalignment of the free-yaw wind turbine. Moreover, the effect of the make-meandering amplitude is more obvious in this figure. As has been stated before, the wake meandering amplitude for the fix-yaw wind turbine with negative yaw input misalignment is higher than the rest. The higher amplitude allows a better wake

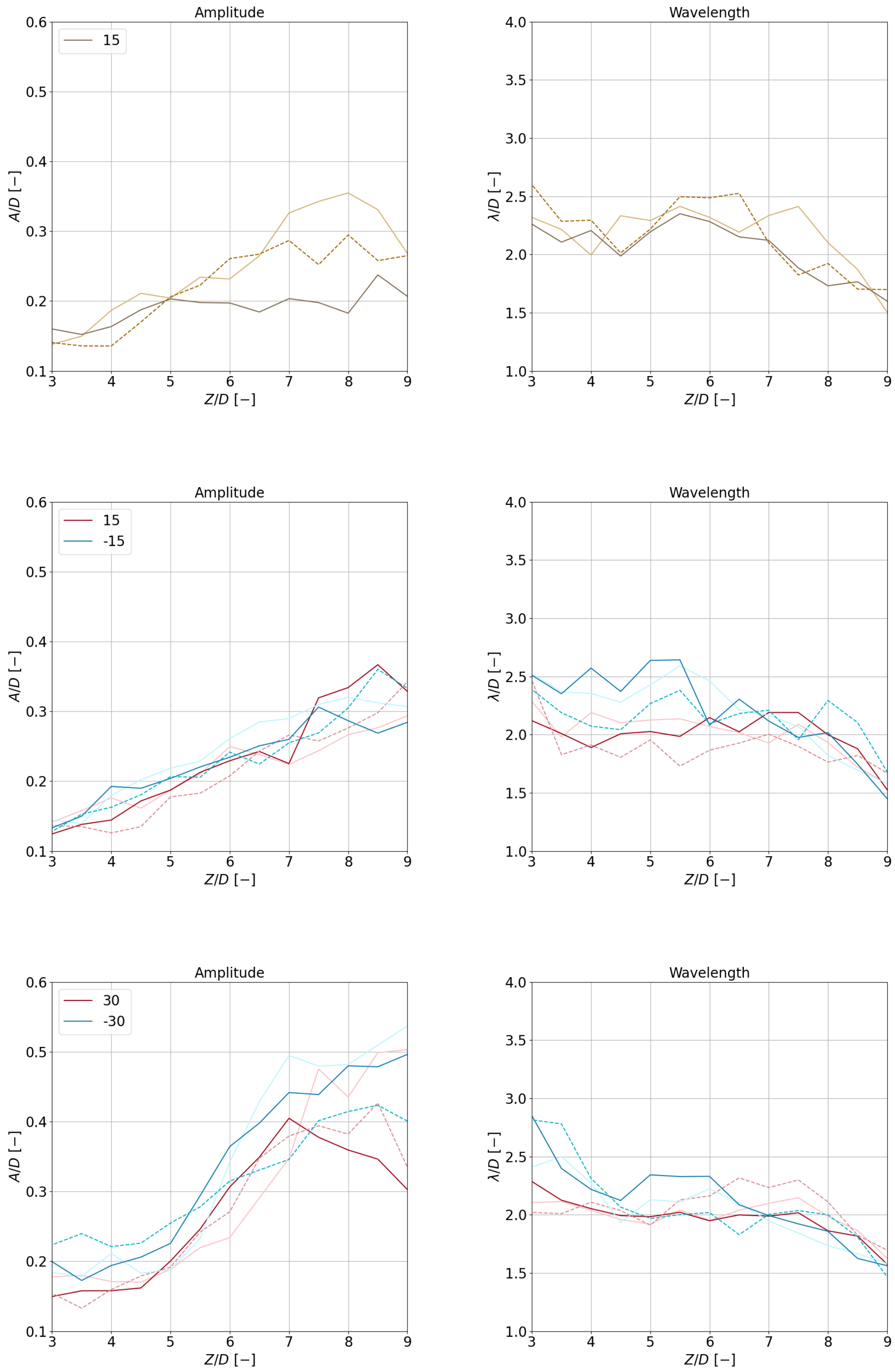

Figure 3.13: Amplitude (left) and wavelength (right) of the far-wake with yaw input misalignment from 0° (top), ±15° (center), and ±30° (bottom). The dark-colored line represents fix-yaw without load-IPC, the light-colored line represents fix-yaw with load-IPC, and the dotted line represents free-yaw with load and yaw-IPC.

mixing and hence a better wake recovery. This leads to an attenuation of the wake deficit peak.

It comes to the interest of knowing the available power that can be harnessed at the downstream locations of the wind turbine where figure 3.15 shows it. In general, the yaw input misalignment allows more power to be captured at the downstream position. Nevertheless, for the free-yaw wind turbine with -15° yaw input misalignment, the available power is reduced. Also, with the yaw input misalignment, the available power downstream, created by the free-yaw wind turbine is inferior to the available power downstream of the fix-yaw wind turbine. The increase of the available power downstream is more notable when the free-yaw wind turbine is misaligned to a positive yaw position. The reduction of the available power of the free-yaw wind turbine with 15° yaw input misalignment is insignificant compared to the fix-yaw. However, this relative difference in the available power grows when the yaw input misalignment goes up. As has been stated earlier, the available power downstream is related to the mean wake velocity deficit profile. Despite the mean velocity profile taking into account only the velocity at hub height, it shows coherence between the mean wake velocity deficit profile with the available power at the downstream position.

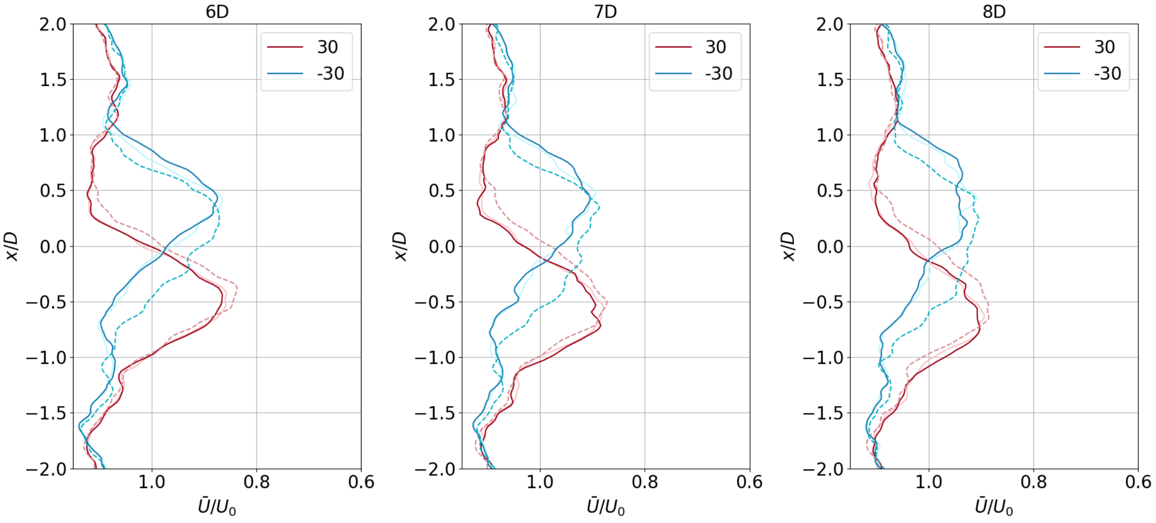

(a): Yaw input misalignment $\pm 30^\circ$

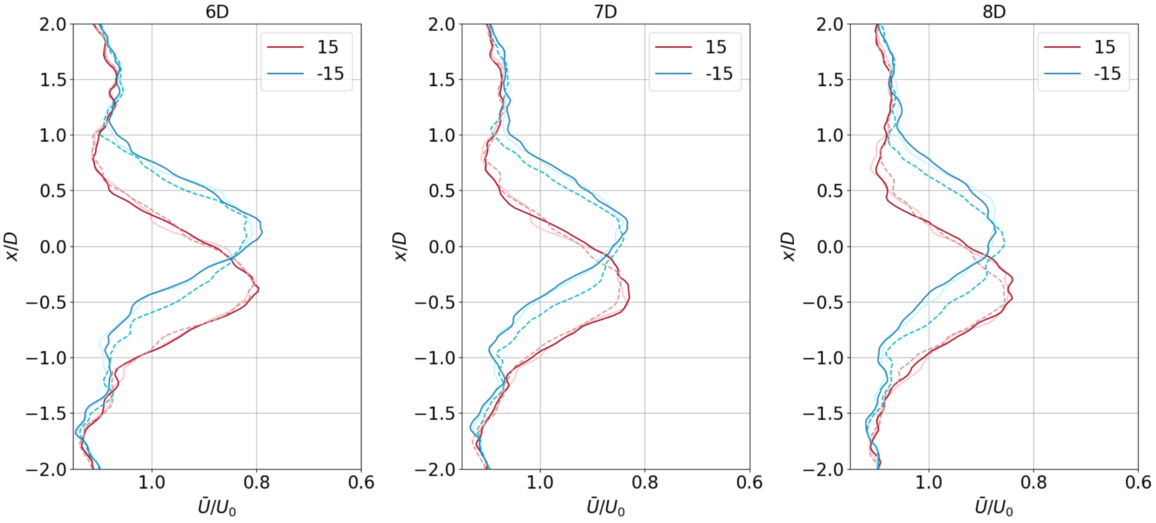

(b): Yaw input misalignment $\pm 15^\circ$

Figure 3.14: Mean velocity profile at 6D, 7D, and 8D (from left to right) downwind location from the rotor with yaw input misalignment of $\pm 30^\circ$ (top) and $\pm 15^\circ$ (bottom), with turbulence. The dark-colored line represents fix-yaw without load-IPC, the light-colored line represents fix-yaw with load-IPC, and the dotted line represents free-yaw with load and yaw-IPC.

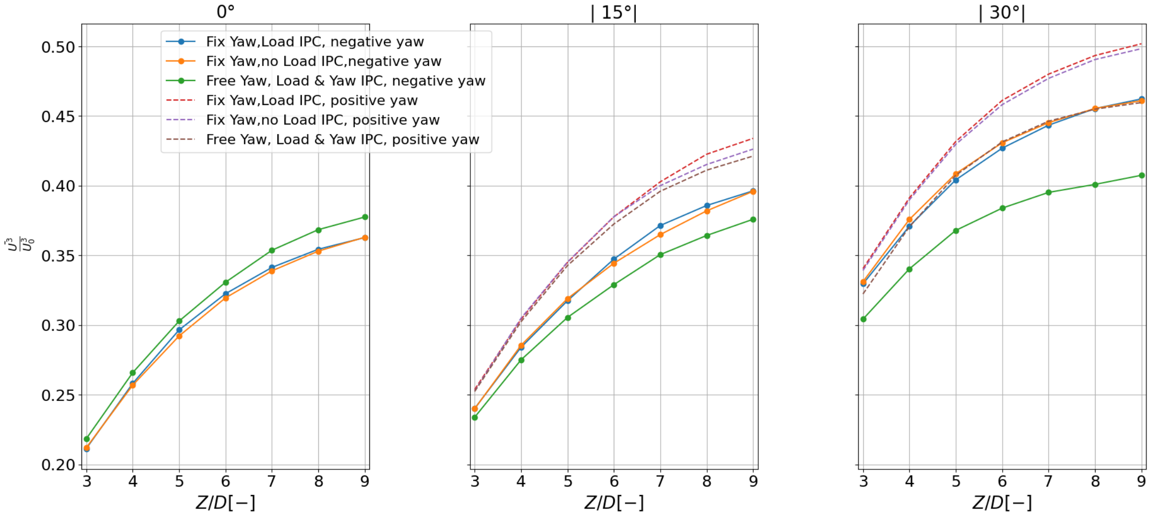

Figure 3.15: Power available at 3D to 9D position downstream. Yaw input misalignment from 0° to ±30° (left to right).

Figure 3.16 shows the time-averaged flap-wise bending moment cycle of the wind turbines. The turbulence increases the average of the flap-wise bending moment in one cycle and the loading imbalance. Despite that, the fix-yaw with load-IPC and the free-yaw show similar evolution of the cyclic flap-wise bending moment with the case without turbulence. In figure 3.17a the DEL of the flap-wise bending moment is shown. The DEL of the flap-wise bending moment of the fix-yaw without load-IPC decreases as the yaw input misalignment is increased. This is due to the decrease of the loading imbalance of the cyclic flap-wise bending moment, portrayed in figure 3.16. This occurrence is also observed in the no turbulence case. The load-IPC manages to reduce the DEL of the flap-wise bending moment for the fix-yaw and the free-yaw wind turbine, although the reduction is not as huge as the cases without turbulence. The DEL of the flap-wise bending moment of the free-yaw and the fix-yaw with load-IPC wind turbines does not depict any clear pattern as a function of its yaw input misalignment. In regards to the free-yaw wind turbine, the DEL of the flap-wise bending moment does not show any symmetry at 0° yaw input misalignment. Despite that, it still increases as it is misaligned except for the -15° yaw input misalignment.

The power production is shown in figure 3.17a. The significance of the turbulence toward the relative difference in the power production between the different wind turbine setups is minimal. The wind turbine that is equipped with load-IPC shows less power generation in most cases. The power generated by the free-yaw wind turbine grows larger than the fix-yaw wind turbine with load-IPC when the yaw input misalignment is increased. This is due to the yaw error of the free-yaw wind turbine.

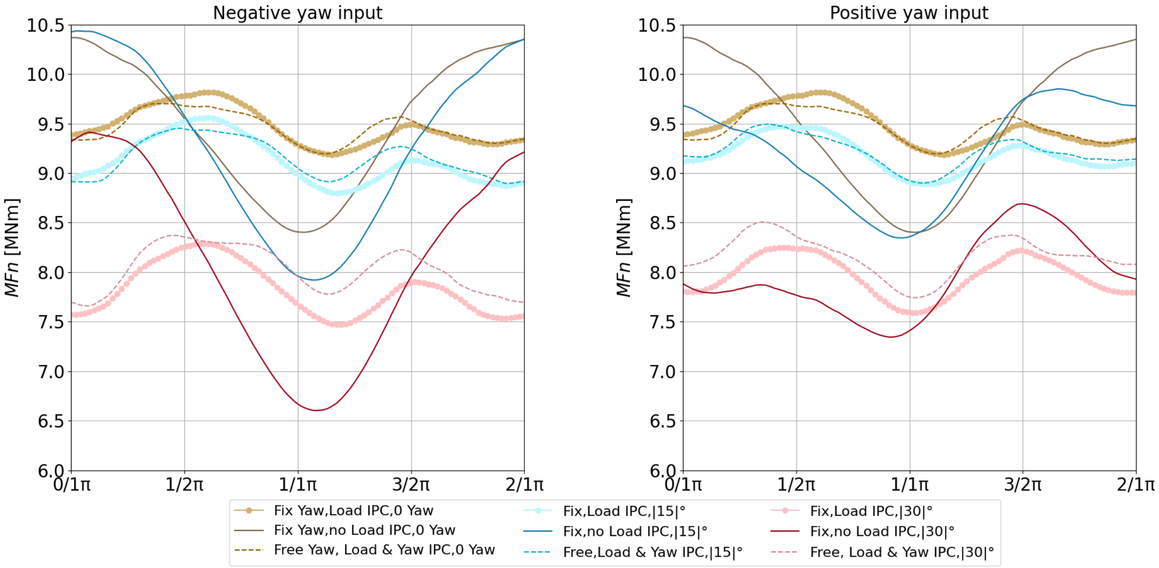

Figure 3.16: Time-averaged flap-wise bending moment cycle for different wind turbine setups and different yaw input misalignment. Averaged within 32 convective times.

The DEL of the tilting moment at the nacelle joint and the DEL of the azimuthal bending moment are shown in figure 3.17b. As observed by [4], the DEL of the azimuthal bending moment is reduced when the load-IPC is engaged for the fix-yaw with load-IPC and the free-yaw wind turbines. The yaw error in the free-yaw wind turbine does not show any signs on the DEL azimuthal bending moment. The DEL of the tilting moment shows that the tilting moment at the nacelle joint of the free-yaw wind turbine is higher than the fix-yaw wind turbine. This observation is expected given the fact that the tilting articulation is set fixed. Consider the case when the wind turbine rotates clockwise while looking down from the y-positive position. The rotational velocity of the yawing wind turbine (or the precessional velocity) creates an angular momentum into the positive y-direction. As mentioned earlier, the anti-clockwise rotation of the rotor creates an angular momentum in the z-positive direction, looking from the downstream position. From these two angular momenta, it yields a net angular momentum as shown in figure 3.18. The vertical component of the angular momentum would tend to rotate the wind turbine nacelle on the negative x-axis (out of the paper) if the articulation is set to free. The constraint in the tilt articulation converts the angular momentum into the form of tilting torque.

The tilting torque is shown in figure 3.19 as a function of time and frequency. The tilting torque is composed of the azimuthal bending moment load, the tilting torque produced by the aerodynamic load, and the tilting torque induced by the yaw rate as has been described earlier. With the help of load-IPC, the tilting torque produced by

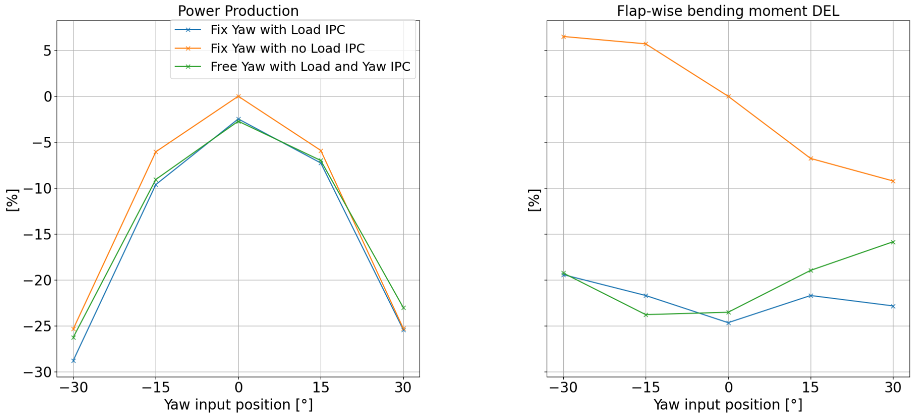

(a): Power production (left) and flap-wise bending moment (right)

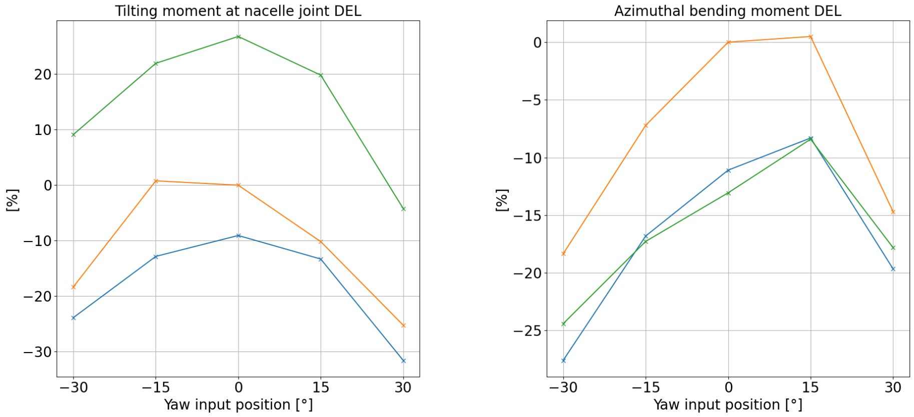

(b): Tilting torque at articulation DEL (left) and azimuthal bending moment (DEL) (right)

Figure 3.17: Power production and the damage equivalent loading (DEL) of wind turbines exposed to turbulence.

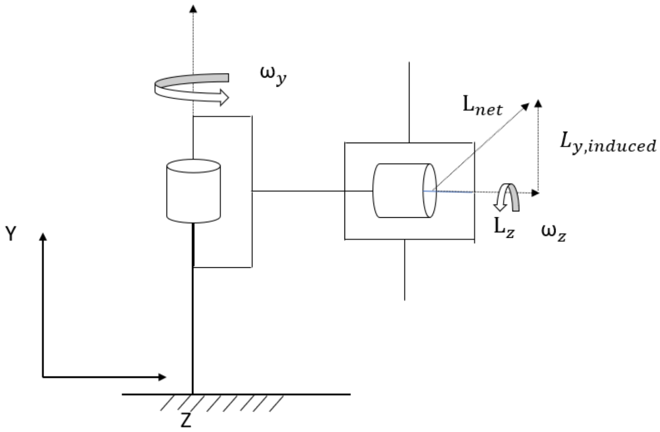

Figure 3.18: Schematic of the induced angular momentum due to yaw rotational speed.

the aerodynamic load is alleviated. By applying *Fast-Fourier-Transform* (FFT) on the tilting torque of a free-yaw wind turbine with load and yaw-IPC, the contribution of the azimuthal bending moment load and the tilting torque induced by the yaw rate can be decomposed. The resonance frequency of the tilting torque can be seen on the right side of figure 3.19b. it shows a similar resonating frequency band between the tilting torque and the yaw speed, which is at the proximity of the $3P$ frequency (3 times per revolution). The tilting torque is measured in the nacelle reference frame, while the azimuthal bending moment is measured in the rotor frame. The projection of the azimuthal bending moment in the nacelle reference frame adds contribution to the tilting torque. The tilting torque is passed through a low-pass filter by applying a moving average and shows that the projected azimuthal bending moment on the nacelle reference frame causes the low frequency of the tilting torque. On the other hand, the oscillating tilting torque is induced by the yaw rate.

The decomposition of the tilting torque by *rainflow* counting for the wind turbine setups at $0°$ yaw input misalignment is given in figure 3.20. It is noticed that the fix-yaw wind turbines (figure 3.20a and 3.20b) have a high occurrence at a low-loading cycle bin. The load-IPC mitigates the high-load cycle. The free-yaw wind turbine shows a half-fold of the low-loading cycle, nevertheless, the increase of the occurrence in higher loading cycle is compelling in the DEL evaluation. In general, the cyclic loading is spread to the high-loading cycle bin, which causes an increase in the DEL of the tilting torque.

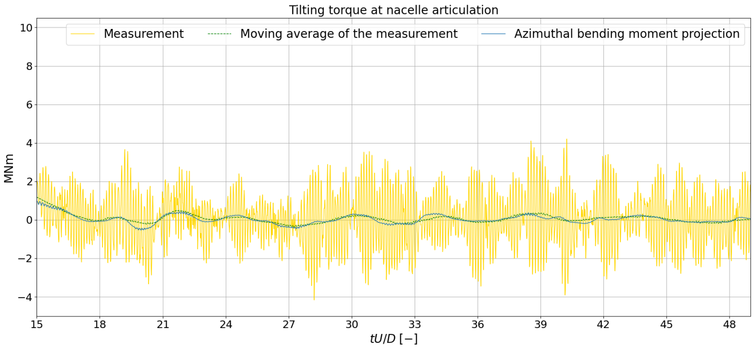

(a): Tilting torque evolution in time domain

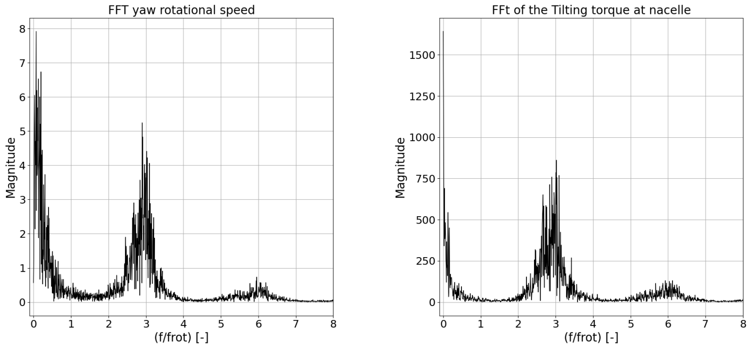

(b): Tilting torque in frequency domain (right) and the yaw rotational speed in frequency domain (left)

Figure 3.19: Free-yaw wind turbine with yaw input misalignment of $0°$ tilting torque and yaw rotational speed.

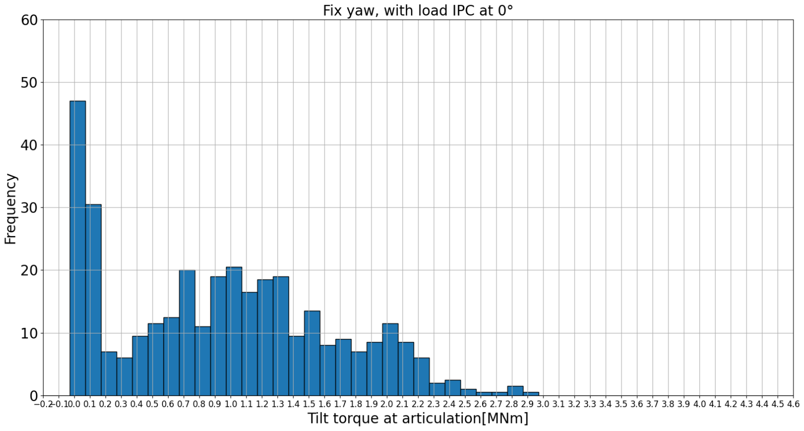

(a): Fix-yaw wind turbine with load-IPC

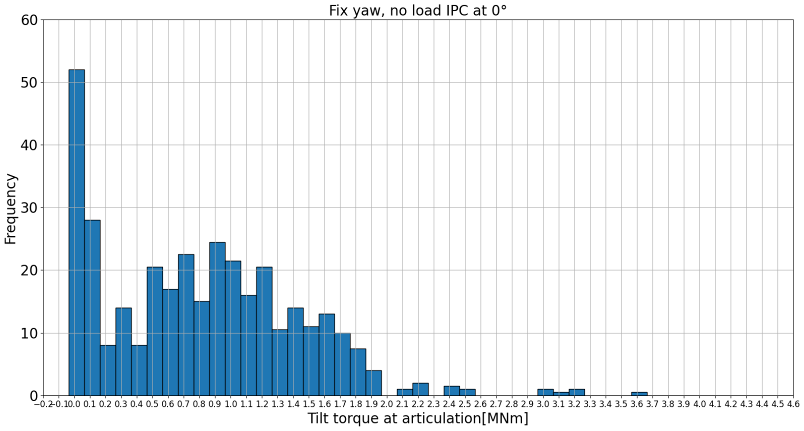

(b): Fix-yaw wind turbine without load-IPC

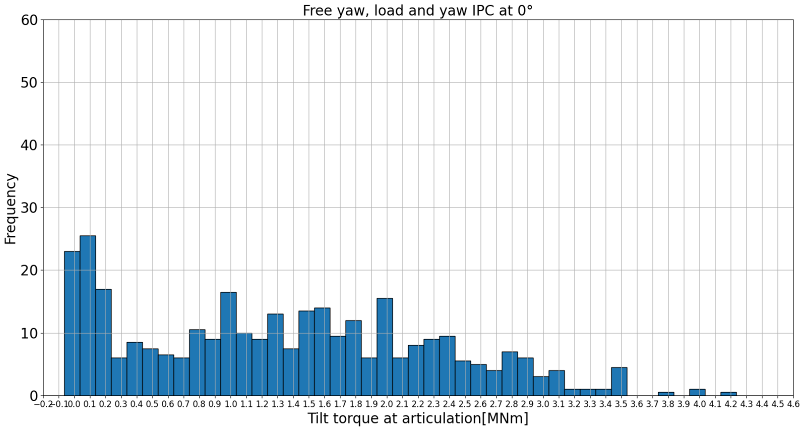

(c): Free-yaw wind turbine with load and yaw-IPC

Figure 3.20: Decomposition of the DEL tilting torque using *rainflow* counting. Yaw input misalignment of 0°.

3.3 Conclusion

This chapter has explained one of the wake mitigation strategies by imposing a static yaw input misalignment to redirect the wake deficit and thus improve the available power to be captured downstream. A free-yaw wind turbine, equipped with load and yaw-IPC, was compared to a fix-yaw wind turbine, with and without load-IPC. In the non-turbulence case, the mechanism of how the wind turbine redirects itself was explained in the case of turbulence absence. It has been shown that a tilting moment is necessary to steer the wind turbine. Although the yaw-IPC is fed in the load-yaw-IPC, the controller creates the steering tilting torque. The yaw-IPC shows a mean static yaw error with a low yaw error standard deviation. Despite this static mean yaw error, the redirection capability did not vary the mean wake center position with respect to the reference case. With respect to the fix-yaw with the load-IPC wind turbine, the static yaw error increased the power production on the free-yaw wind turbine. The load-IPC reduced the load imbalance of the cyclic flap-wise bending moment for the free-yaw and the fix-yaw wind turbines, which reduced The DEL of the flap-wise bending moment.

Afterward, the cases with turbulence were investigated. With the turbulence, the free-yaw wind turbine became more unstable, yet the yaw error can still be accepted. Regarding the wake, the deviation of the mean wake center positions of the free-yaw wind turbine was caused by the yaw error. The amplitudes and the wavelength were not affected by the yaw error, where this finding is supported by [21]. The amplitude allows better wake-mixing at the downstream position and thus reduces the wake velocity deficit. The available power was affected by the distribution of the wake velocity deficit on the lateral position. The mean wake center position plays a big role in the determination of the wake velocity deficit extrema position. With the presented mean wake velocity deficit profile, the free-yaw wind turbine yielded less available power at the downstream position when it was misaligned. The power production showed a similar profile between different wind turbine setups with the no-turbulence case. The load-IPC was able to mitigate the flap-wise bending moment. The DEL of the tilting torque was investigated and showed that the free-yaw wind turbine suffered a higher loading due to a few occurrences of a high-loading cycle.

The next chapter will discuss another wake mitigation strategy where the yaw input misalignment varies through time. From this chapter one can already see a glance of this strategy as the free-yaw wind turbine could not maintain a static yaw position.

Chapter 4

Dynamic yaw input misalignment

4.1 Introduction

Dynamic yaw misalignment is another strategy to mitigate the wake downstream. In the previous section, the free-yaw wind turbine showed dynamic yaw behavior and its outcomes, although the wind turbine was imposed with static yaw input misalignment. Dynamic yaw misalignment strategy was investigated by [4] where a free-yaw wind turbine was allowed to yaw freely without any yaw control, yet with and without load-alleviating IPC. [17] investigated a fix-yaw wind turbine that is allowed to exceed its normal operating yaw rate. They found a slight benefit in comparison to static wake redirection.

As has been mentioned in section 1.3 axial induction control is another means to mitigate the wake downstream. This strategy aims to optimize the induction factor with the help of the IPC. [22] investigated a periodic dynamic induction control (PDIC) where the induction factor of the upstream wind turbine is enhanced so that the wake mixing downstream can be improved. Nevertheless, this strategy escalated the fatigue loads and produced moderate power gains [23].

Aside from the increase of the DEL of the tilting moment in the nacelle joint, the absence of a yaw actuator allows the wind turbine to rotate faster than a fix-yaw wind turbine operating yaw rate. [22] and [23] imposed a periodic frequency that is described by the dimensionless Strouhal number of 0.25 where $St = \frac{f_e D}{U_0}$ where f_e is the frequency, D is the diameter of the wind turbine, and U_0 is the free-stream velocity. This frequency has been shown to be the optimal frequency to increase the wake mixing intensity. In this chapter, the wind turbine is investigated to oscillate with the aforementioned frequency with the expectation to increase the wake mixing intensity. The goal is to observe the implication of an oscillating wind turbine in regard to its wake and its loading. The yaw input misalignment can be mathematically expressed as in equation (4.1).

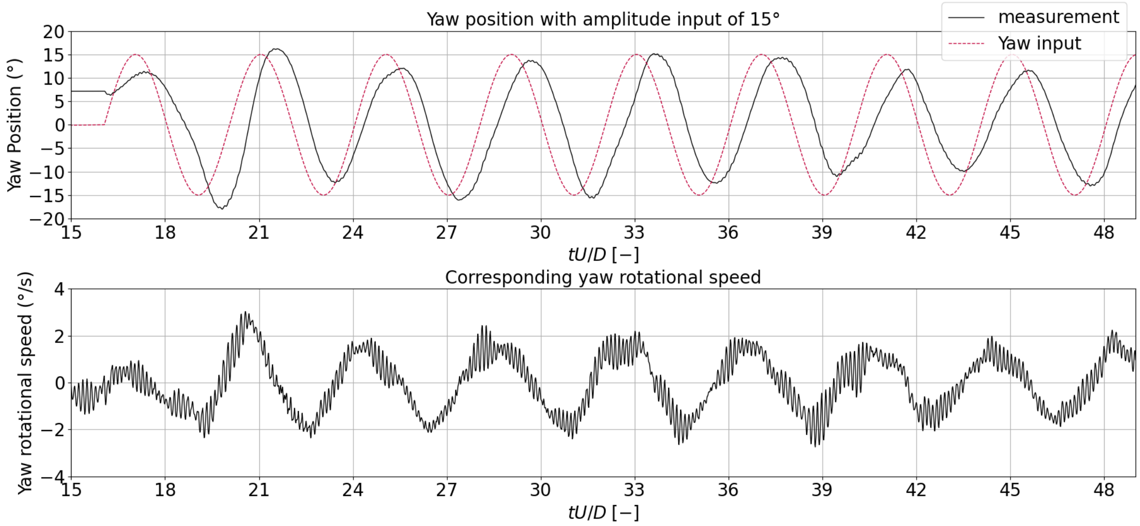

Figure 4.1: Yaw position evolution (top) and the corresponding yaw rotational speed (bottom) with excitation amplitude of $15°$

$$\gamma_{\text{input}} = \gamma_{\text{ref}} + A\ sin(\omega(t - t_{\textit{IPC,start}})) = \gamma_{\text{ref}} + A\ sin(2\pi St\frac{U_0}{D}(t - t_{\textit{IPC,start}})) \tag{4.1}$$

γ_{ref} is the offset yaw input misalignment, A is the amplitude, and $t_{\textit{IPC,start}}$ is the time where the yaw-IPC is engaged. The simulated amplitude of the excitation in [23] was 2.5° where this amplitude corresponds to the optimal parameter in PDIC. This chapter will vary the amplitude of 2.5°, 8.0°, and 15.0°. The amplitude of $15°$ is chosen based on the static yaw input misalignment result, while 2.5° is chosen based on [23]. The intermediary angle is chosen arbitrarily. The offset yaw input misalignment is set to 0°.

4.2 Results

Figure A.4 shows the evolution of the yaw position and the yaw rate against the normalized time domain. one can observe the delay between the yaw input and the corresponding yaw position, and the turbulence causes the yaw position to exceed or fall behind the desired amplitude. Despite that, the yaw position profile acts upon the yaw input desired frequency. In comparison to the static yaw input misalignment with turbulence, the yaw rate contains the excitation frequency. The yaw rate magnitude is in the acceptable range.

The mean wake center positions and their standard deviation are depicted in figure 4.2. The free-yaw wind turbines enhance the capability to redirect the wake further

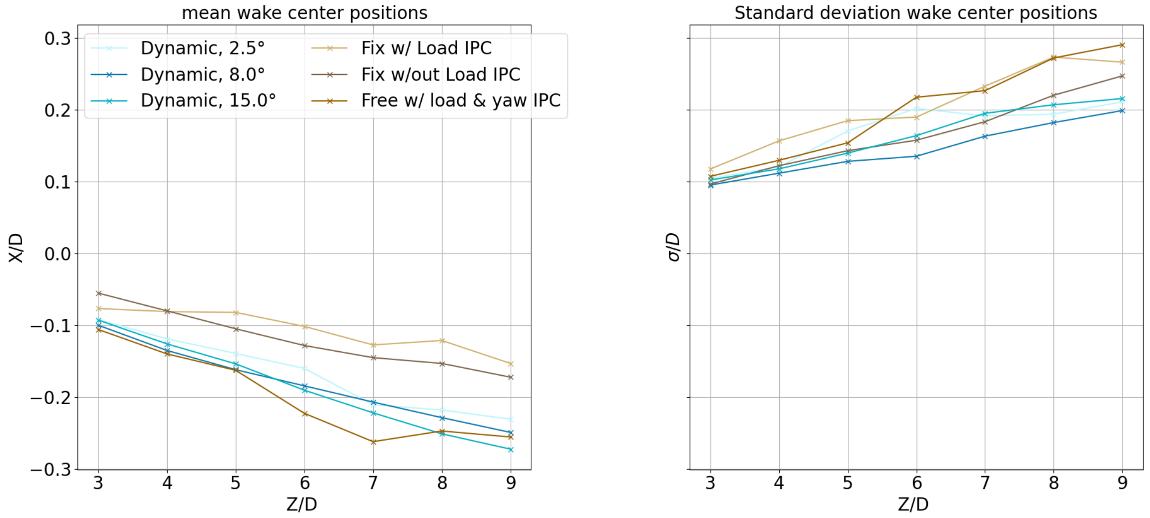

Figure 4.2: Mean wake center position (left) and the standard deviation (right) between the dynamic yaw input misalignment (blue) and the static yaw input misalignment (brown). Measured from $3D$ to $9D$ downstream from the rotor

from the center-line position, yet, the free-yaw wind turbine with dynamic yaw input misalignment attenuates the wake-meandering effect in the far-wake region. This can be seen as the standard deviation's growth of the dynamic yaw input wind turbine cases is inferior to the static yaw input misaligned free-yaw wind turbine. The wake meandering characteristics are shown in figure 4.3a. In most cases, The wake meandering characteristic of the dynamic yaw input misalignment shows no significance in comparison to the free-yaw static yaw input misalignment. The intermediary amplitude (8°) shows the lowest amplitude although it appears to have the same amplitude growth rate with the dynamic yaw input misalignment setups as it progresses to the downstream location. The wavelength of the dynamic yaw input wind turbines shows a shorter wavelength at 5D to 7D downstream locations, yet there is no real conclusion that can be made.

The mean velocity profile can be seen in figure 4.3b. The free-yaw wind turbines deviate the wake velocity deficit extremum position further from the center line than the fix-yaw wind turbine. This phenomenon correlates to the mean wake center position as has been explained in section 3.2. Among the other dynamic yaw input wind turbines, the mean velocity profile of the dynamic yaw input wind turbine with 15° amplitude shows a better wake mixing creating a marginally lower wake velocity deficit. The mean velocity profile of the 8° amplitude setup shows the highest wake deficit.

The available power downstream is depicted in figure 4.4. It is clear that the dynamic yaw input reduces the power available downstream. The highest amplitude of the dynamic yaw input yields the highest available power downstream among other

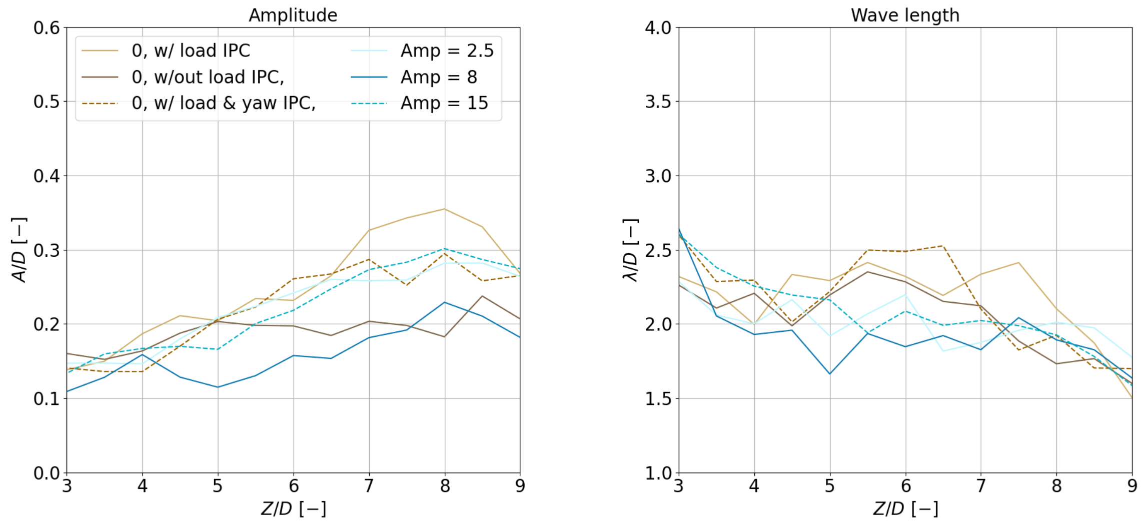

(a): Amplitude (left) and wavelength (right) of the dynamic yaw input (blue) and the static yaw input(brown) misalignment

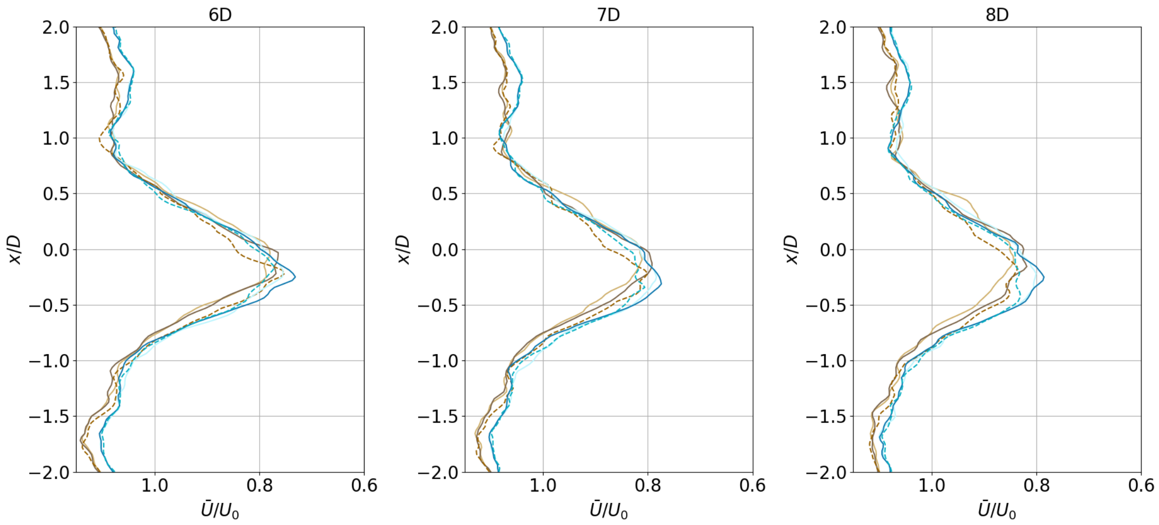

(b): Mean velocity profile at $6D$, $7D$, and $8D$ (from left to right) downwind location from the rotor. Dynamic yaw input (blue) and the static yaw input(brown) misalignment.

Figure 4.3: The wake-meandering characteristics (top) and the mean velocity profile (bottom)

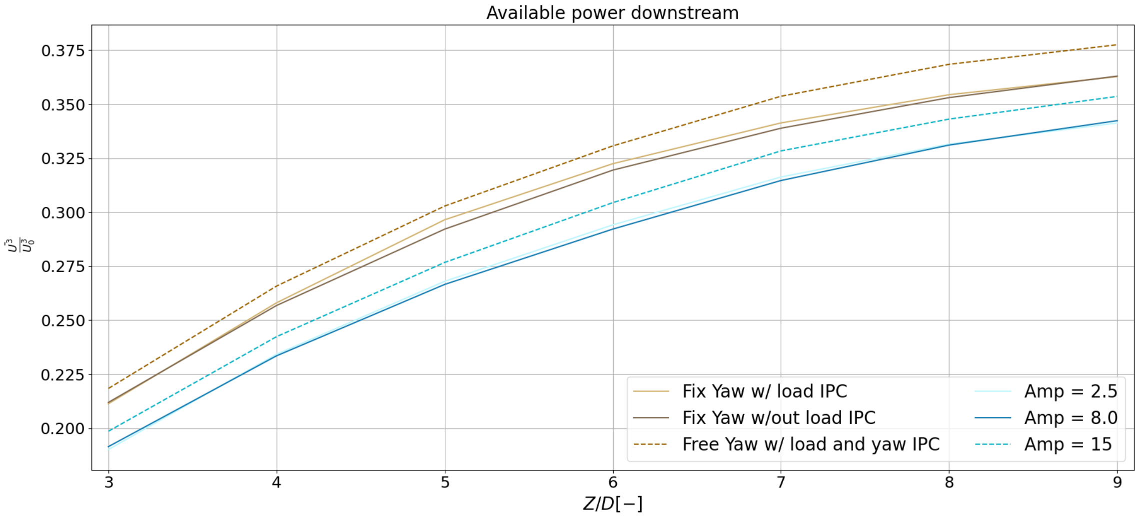

Figure 4.4: Available power at $3D$ to $9D$ position downstream

dynamic yaw input setups. Although the mean wake center position of the wind turbine with dynamic yaw input is located further from the center line, the wake deficit effect reduces the power available downstream.

As shown in figure 4.5a, the imposed dynamic yaw input misalignment wind turbines generate less power as the rotor plane is not aligned with the incoming wind. The higher the amplitudes, the less power it can capture. The load-IPC mitigates the DEL of the flap-wise bending moment of the dynamic yaw input wind turbine, while the increase in amplitude rises it. Although the purpose of the load-IPC is not to mitigate the azimuthal bending moment, again, it appears that the azimuthal bending moment of the dynamic yaw input misalignment is reduced. The DEL of the tilting torque of a free-yaw wind turbine is increased due to the aforementioned reason, nevertheless, the DEL of the dynamic yaw input wind turbine is less severe than the static yaw input free-yaw wind turbine. This can be seen in figure 4.5b. The decomposition of the DEL of the tilting torque of the dynamic yaw input wind turbine is shown in figure 4.6. In comparison to the static yaw input wind turbine, the occurrence of the low-load cycle is higher while the high-load cycle is less. This explains the lower DEL of the tilting torque of the dynamic yaw input misalignment. As the amplitude increases, the tilting torque is more prone to a high-load cycle.

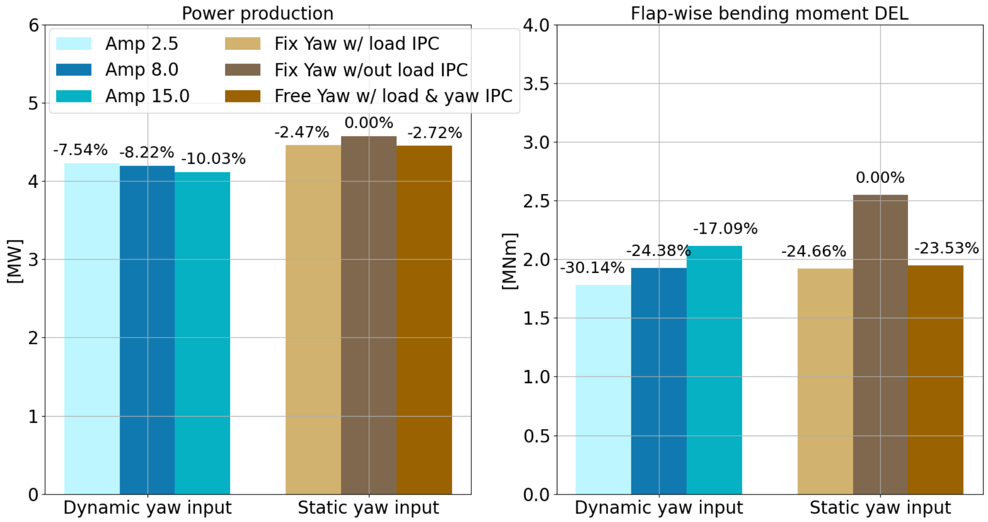

(a): Power production (left) and flap-wise bending moment (right)

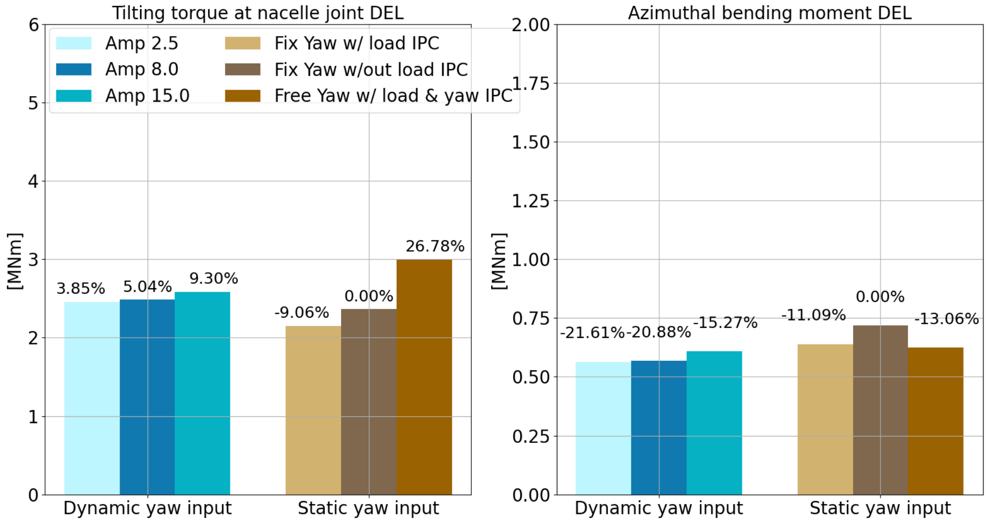

(b): Tilting torque at articulation DEL (left) and azimuthal bending moment (DEL) (right)

Figure 4.5: Power production and the damage equivalent loading (DEL) of wind turbines exposed to turbulence.

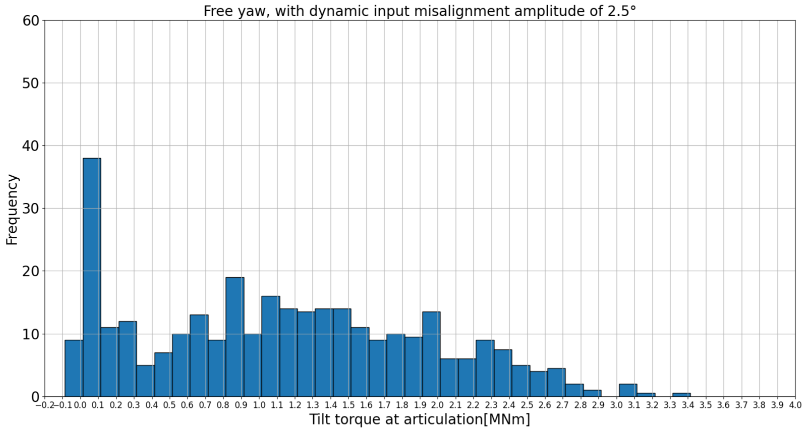

(a): dynamic yaw input, $2.5°$ amplitude

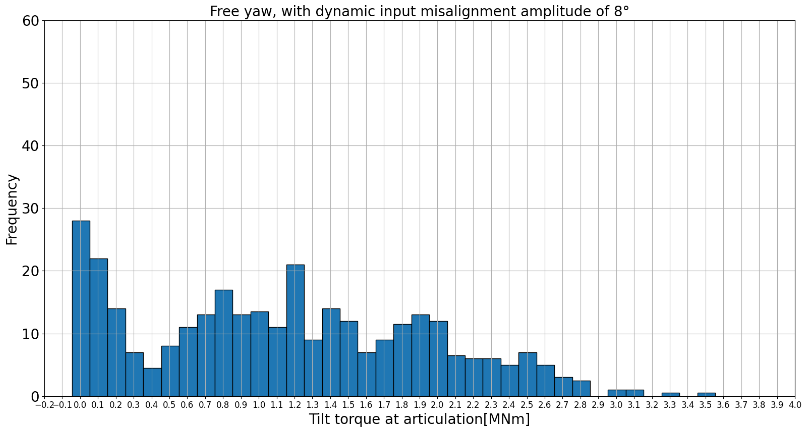

(b): dynamic yaw input, $8.0°$ amplitude

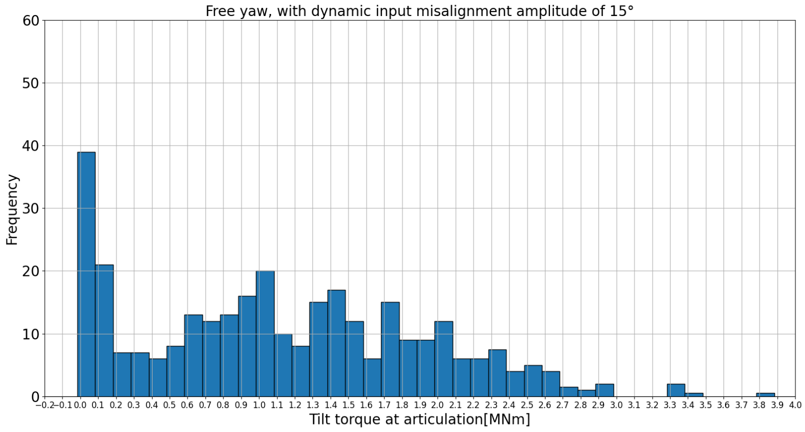

(c): dynamic yaw input, $15.0°$ amplitude

Figure 4.6: Decomposition of the DEL tilting torque using *rainflow* counting. dynamic yaw input misalignment setups

4.3 Conclusion

This chapter has investigated the effect of an oscillating free-yaw wind turbine with the desired frequency. The yaw-IPC accomplished to oscillate the wind turbine with the desired frequency despite the shortcomings. The oscillating wind turbine appeared to shift the wake center mean position yet it attenuated the wake-meandering and reduced the intensity of the wake mixing. The available power that can be harnessed at the downstream position is lower in comparison to the fix-yaw wind turbine and the free-yaw wind turbine with static yaw input misalignment. In regards to the generated power, the oscillating wind turbine produced less power as it misaligned the rotor plane with the incoming wind. The flap-wise bending moment load of the dynamic yaw input wind turbine is alleviated by the load-IPC, yet higher amplitude input increase the severity of the loading. The tilting torque loading is reduced as the wind turbine experienced a higher low-load cycle and less high-load cycle. In conclusion, the oscillating free-yaw wind turbine does not show any significance in increasing the intensity of the wake mixing despite its ability to redirect the wake compared to the fix-yaw wind turbine.

Chapter 5

Conclusion and perspectives

Power optimization of a wind farm has become one of many main interests in the field of renewable energy. Many strategies were proposed and wake redirection is one of the promising strategies. Wake redirection can be achieved by misaligning the yaw position of the wind turbine from the incoming wind. However, this strategy causes loads that act upon the yaw actuator of a fix-yaw wind turbine. This leads to the reduction of its lifetime. One of the solutions is a free-yaw wind turbine. This master thesis has presented a free-yaw wind turbine, equipped with a yaw controller, to create the misalignment with the incoming wind. The wake and the loads were analyzed. Two strategies were studied, namely; static yaw input and dynamic yaw input.

In the first chapter, the context and motivation were explained. By its nature, a free-yaw wind turbine is a setup that alleviates the load that acts on the yaw actuator, which is normally installed in a commercial fix-yaw wind turbine. The goal of this master's thesis was addressed. To sum up, the IPC was exploited to control or steer the yaw position of the wind turbine.

Chapter Two addressed the methodology of this master thesis. Vortex Particle-mesh Method (VPM) was used to solve the flow in the simulation. To analyze the loads and the dynamic of the wind turbine ROBOTRAN was used. The coupling of VPM and ROBOTRAN was briefly explained. Afterward, the wind turbine parameters were given, along with the controller. At this moment, the yaw-IPC was introduced. Damage Equivalent Loading (DEL) evaluated the loads. Thanks to *rainflow* counting, different bins of cyclic loads can be grouped. The wake tracking method that had been presented by [14], was used. From this wake tracking, the wake meandering characteristics were evaluated. Finally, the numerical setup of this master thesis was explained.

In chapter three a static yaw input misalignment case was investigated. First, the case where no turbulence was presented. In the transient period, it was shown that the yaw-IPC steered the yaw of the wind turbine by creating a tilting torque. Despite the yaw-IPC was fed into the load-yaw IPC, it still generated the necessary tilting torque.

At steady state, the yaw-IPC could not attain the desired yaw input and created a static yaw error. Despite this, the wake characteristic depicted a similar profile to the fix-yaw wind turbine in most cases. Next, the turbulence was added to the simulation. With the turbulence, it increased the mean yaw error and the yaw error standard deviation. Due to this yaw error, the mean wake center position of the free-yaw wind turbine deviated. The wake meandering characteristics; the amplitude and the wavelength, were not affected by the yaw error. The power available created by the free-yaw wind turbine was less when it was misaligned. The turbulence also created higher tilting torque due to the yaw rate.

In the last chapter, the dynamic yaw input was implemented. This strategy was studied with the hope to increase the wake mixing intensity. The free-yaw wind turbine oscillated with the frequency that was used in the periodic dynamic induction control (PDIC) strategy. The yaw-IPC managed to oscillate the wind turbine with the desired frequency despite the shortcomings. This strategy appeared to attenuate the wake meandering effect as the standard deviation of the wake center position decreased. This strategy showed less available power at the position downstream in comparison to the static yaw input misalignment. In regard to power production, dynamic yaw input misalignment generated less power. The wind turbine wind with higher oscillation amplitude suffered the most flap-wise bending moment load, yet the tilting torque was reduced.

The performance and drawbacks of a free-yaw wind turbine have been summarized above. The free-yaw wind turbine is more promising with the static yaw input misalignment aside from the higher DEL of the tilting torque in comparison to the fix-yaw wind turbine. Nevertheless, further study still needs to be done. It would be great to be able to identify which type of load has a greater impact on the lifecycle of a wind turbine. Another aspect to be investigated is the aggressiveness of the controller. It can be further investigated in the hope to minimize the yaw error. For the dynamic yaw input misalignment, other excitation frequencies can be tested.

Bibliography

[1] A. Hansen, “Yaw dynamics of horizontal axis wind turbines. final report,” May 1992.

[2] G. Wanke, M. H. Hansen, and T. J. Larsen, “Qualitative yaw stability analysis of free-yawing downwind turbines,” *Wind Energy Science*, vol. 4, no. 2, p. 233–250, 2019.

[3] S. Boersma, B. Doekemeijer, P. Gebraad, P. Fleming, J. Annoni, A. Scholbrock, J. Frederik, and J.-W. van Wingerden, “A tutorial on control-oriented modeling and control of wind farms,” *2017 American Control Conference (ACC)*, 2017.

[4] J.-B. Crismer, “Numerical study of the effect of individual pitch control and yaw dynamics on wind turbines wakes and loads,” 2021.

[5] E. A. Bossanyi, “Individual blade pitch control for load reduction,” *Wind Energy*, vol. 6, no. 2, p. 119–128, 2003.

[6] S. T. Navalkar, J. W. van Wingerden, and G. A. van Kuik, “Individual blade pitch for yaw control,” *Journal of Physics: Conference Series*, vol. 524, 2014.

[7] S. Backaert, P. Chatelain, and G. Winckelmans, “Vortex particle-mesh with immersed lifting lines for aerospace and wind engineering,” *Procedia IUTAM*, vol. 18, p. 1–7, 2015.

[8] P. Chatelain, S. Backaert, G. Winckelmans, and S. Kern, “Large eddy simulation of wind turbine wakes,” *Flow, Turbulence and Combustion*, vol. 91, no. 3, p. 587–605, 2013.

[9] P. Chatelain and P. Koumoutsakos, “A fourier-based elliptic solver for vortical flows with periodic and unbounded directions,” *Journal of Computational Physics*, vol. 229, no. 7, p. 2425–2431, 2010.

[10] P. Chatelain, A. Curioni, M. Bergdorf, D. Rossinelli, W. Andreoni, and P. Koumoutsakos, “Billion vortex particle direct numerical simulations of aircraft wakes,” *Computer Methods in Applied Mechanics and Engineering*, vol. 197, no. 13-16, p. 1296–1304, 2008.

[11] J. Mann, “The spatial structure of neutral atmospheric surface-layer turbulence,” *Journal of Fluid Mechanics*, vol. 273, p. 141–168, 1994.

[12] P. Fisette and N. Docquier, *Modelling Multibody Systems with ROBOTRAN*. 2020.

[13] S. Buffin, “Simulation of rotorcraft dynamics through the coupling of a multibody solver and a vortex particle-mesh method,” *Master Thesis, Université Catholique de Louvain*, 2016.

[14] N. Coudou, “Numerical and experimental investigations of the meandering phenomenon in wind turbine wakes,” *PhD Thesis, University of Louvain-la-Neuve, University of Mons, von Karman Institute for Fluid Dynamics*, 2021.

[15] G. Freebury and W. Musial, “Determining equivalent damage loading for full-scale wind turbine blade fatigue tests,” *2000 ASME Wind Energy Symposium*, 2000.

[16] F. Porté-Agel, M. Bastankhah, and S. Shamsoddin, “Wind-turbine and wind-farm flows: A review,” *Boundary-Layer Meteorology*, vol. 174, no. 1, p. 1–59, 2019.

[17] W. Munters and J. Meyers, “Dynamic strategies for yaw and induction control of wind farms based on large-eddy simulation and optimization,” *Energies*, vol. 11, no. 1, p. 177, 2018.

[18] G. España, S. Aubrun, S. Loyer, and P. Devinant, “Wind tunnel study of the wake meandering downstream of a modelled wind turbine as an effect of large scale turbulent eddies,” *Journal of Wind Engineering and Industrial Aerodynamics*, vol. 101, p. 24–33, 2012.

[19] M. Bastankhah and F. Porté-Agel, “Wind tunnel study of the wind turbine interaction with a boundary-layer flow: Upwind region, turbine performance, and wake region,” *Physics of Fluids*, vol. 29, no. 6, p. 065105, 2017.

[20] M. Bastankhah and F. Porté-Agel, “A new analytical model for wind-turbine wakes,” *Renewable Energy*, vol. 70, p. 116–123, 2014.

[21] A. Crespo, J. Hernández, and S. Frandsen, “Survey of modelling methods for wind turbine wakes and wind farms,” *Wind Energy*, vol. 2, no. 1, p. 1–24, 1999.

[22] J. A. Frederik, B. M. Doekemeijer, S. P. Mulders, and J. Wingerden, “The helix approach: Using dynamic individual pitch control to enhance wake mixing in wind farms,” *Wind Energy*, vol. 23, no. 8, p. 1739–1751, 2020.

[23] M. Coquelet, M. Moens, L. Bricteux, J.-B. Crismer, and P. Chatelain, “Performance assessment of wake mitigation strategies,” *Journal of Physics: Conference Series*, vol. 2265, no. 3, p. 032078, 2022.

Appendix A

Static yaw input

A.1 Without turbulence

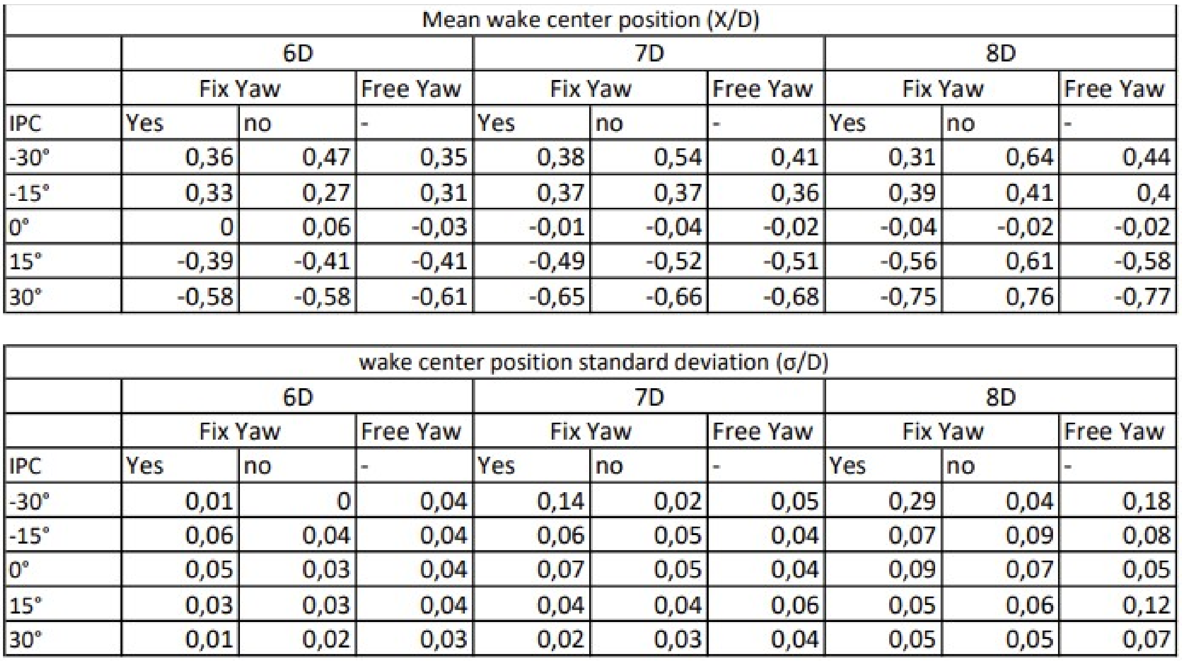

Mean wake center position (X/D)									
	6D			7D			8D		
	Fix Yaw		Free Yaw	Fix Yaw		Free Yaw	Fix Yaw		Free Yaw
IPC	Yes	no	-	Yes	no	-	Yes	no	-
-30°	0,36	0,47	0,35	0,38	0,54	0,41	0,31	0,64	0,44
-15°	0,33	0,27	0,31	0,37	0,37	0,36	0,39	0,41	0,4
0°	0	0,06	-0,03	-0,01	-0,04	-0,02	-0,04	-0,02	-0,02
15°	-0,39	-0,41	-0,41	-0,49	-0,52	-0,51	-0,56	0,61	-0,58
30°	-0,58	-0,58	-0,61	-0,65	-0,66	-0,68	-0,75	0,76	-0,77

wake center position standard deviation (σ/D)									
	6D			7D			8D		
	Fix Yaw		Free Yaw	Fix Yaw		Free Yaw	Fix Yaw		Free Yaw
IPC	Yes	no	-	Yes	no	-	Yes	no	-
-30°	0,01	0	0,04	0,14	0,02	0,05	0,29	0,04	0,18
-15°	0,06	0,04	0,04	0,06	0,05	0,04	0,07	0,09	0,08
0°	0,05	0,03	0,04	0,07	0,05	0,04	0,09	0,07	0,05
15°	0,03	0,03	0,04	0,04	0,04	0,06	0,05	0,06	0,12
30°	0,01	0,02	0,03	0,02	0,03	0,04	0,05	0,05	0,07

Figure A.1: Mean wake center position and the wake center position standard deviation.

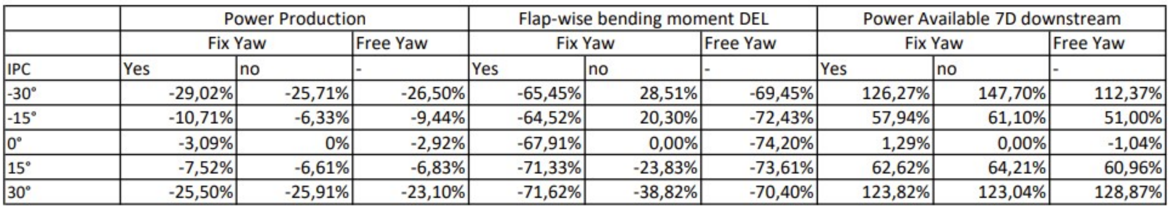

	Power Production			Flap-wise bending moment DEL			Power Available 7D downstream		
	Fix Yaw		Free Yaw	Fix Yaw		Free Yaw	Fix Yaw		Free Yaw
IPC	Yes	no	-	Yes	no	-	Yes	no	-
-30°	-29,02%	-25,71%	-26,50%	-65,45%	28,51%	-69,45%	126,27%	147,70%	112,37%
-15°	-10,71%	-6,33%	-9,44%	-64,52%	20,30%	-72,43%	57,94%	61,10%	51,00%
0°	-3,09%	0%	-2,92%	-67,91%	0,00%	-74,20%	1,29%	0,00%	-1,04%
15°	-7,52%	-6,61%	-6,83%	-71,33%	-23,83%	-73,61%	62,62%	64,21%	60,96%
30°	-25,50%	-25,91%	-23,10%	-71,62%	-38,82%	-70,40%	123,82%	123,04%	128,87%

Figure A.2: Power production, flap-wise bending moment DEL and available power at 7D downstream position.

A.2 With turbulence

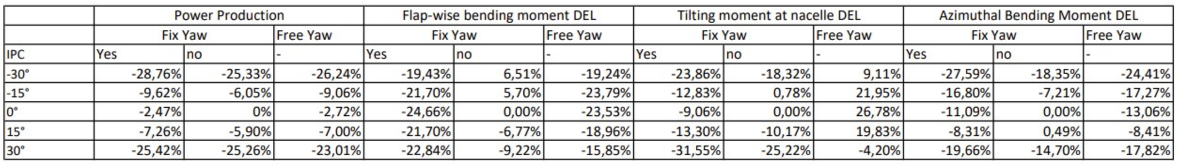

	Power Production			Flap-wise bending moment DEL			Tilting moment at nacelle DEL			Azimuthal Bending Moment DEL		
	Fix Yaw		Free Yaw	Fix Yaw		Free Yaw	Fix Yaw		Free Yaw	Fix Yaw		Free Yaw
IPC	Yes	no	-	Yes	no	-	Yes	no	-	Yes	no	-
-30°	-28,76%	-25,33%	-26,24%	-19,43%	6,51%	-19,24%	-23,86%	-18,32%	9,11%	-27,59%	-18,35%	-24,41%
-15°	-9,62%	-6,05%	-9,06%	-21,70%	5,70%	-23,79%	-12,83%	0,78%	21,95%	-16,80%	-7,21%	-17,27%
0°	-2,47%	0%	-2,72%	-24,66%	0,00%	-23,53%	-9,06%	0,00%	26,78%	-11,09%	0,00%	-13,06%
15°	-7,26%	-5,90%	-7,00%	-21,70%	-6,77%	-18,96%	-13,30%	-10,17%	19,83%	-8,31%	0,49%	-8,41%
30°	-25,42%	-25,26%	-23,01%	-22,84%	-9,22%	-15,85%	-31,55%	-25,22%	-4,20%	-19,66%	-14,70%	-17,82%

Figure A.3: Power production, flap-wise bending moment, tilting torque and azimuthal bending moment.

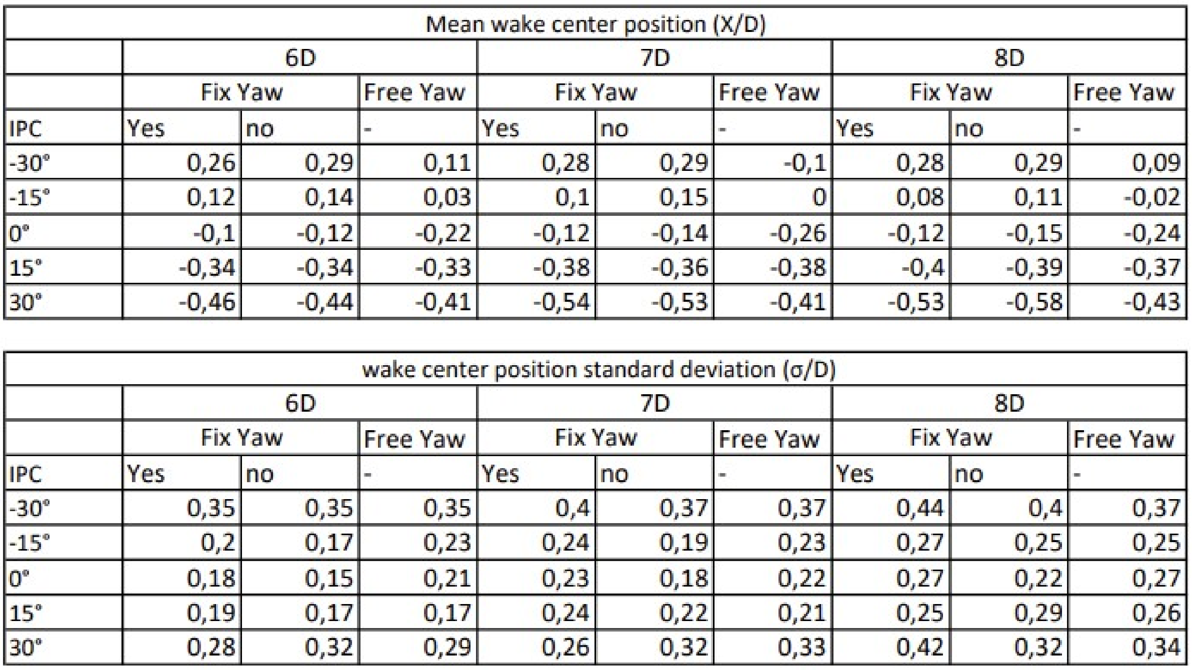

Mean wake center position (X/D)									
	6D			7D			8D		
	Fix Yaw		Free Yaw	Fix Yaw		Free Yaw	Fix Yaw		Free Yaw
IPC	Yes	no	-	Yes	no	-	Yes	no	-
-30°	0,26	0,29	0,11	0,28	0,29	-0,1	0,28	0,29	0,09
-15°	0,12	0,14	0,03	0,1	0,15	0	0,08	0,11	-0,02
0°	-0,1	-0,12	-0,22	-0,12	-0,14	-0,26	-0,12	-0,15	-0,24
15°	-0,34	-0,34	-0,33	-0,38	-0,36	-0,38	-0,4	-0,39	-0,37
30°	-0,46	-0,44	-0,41	-0,54	-0,53	-0,41	-0,53	-0,58	-0,43

wake center position standard deviation (σ/D)									
	6D			7D			8D		
	Fix Yaw		Free Yaw	Fix Yaw		Free Yaw	Fix Yaw		Free Yaw
IPC	Yes	no	-	Yes	no	-	Yes	no	-
-30°	0,35	0,35	0,35	0,4	0,37	0,37	0,44	0,4	0,37
-15°	0,2	0,17	0,23	0,24	0,19	0,23	0,27	0,25	0,25
0°	0,18	0,15	0,21	0,23	0,18	0,22	0,27	0,22	0,27
15°	0,19	0,17	0,17	0,24	0,22	0,21	0,25	0,29	0,26
30°	0,28	0,32	0,29	0,26	0,32	0,33	0,42	0,32	0,34

Figure A.4: Mean wake center position and the wake center position standard deviation.

UNIVERSITÉ CATHOLIQUE DE LOUVAIN
École polytechnique de Louvain
Rue Archimède, 1 bte L6.11.01, 1348 Louvain-la-Neuve, Belgique | **www.uclouvain.be/epl**